

# Contents

|            |   |           |
|------------|---|-----------|
| <b>1</b>   | <b>Measurement of the jet transverse-momentum resolution</b>                  | <b>1</b>  |
| <b>1.1</b> | <b>Introduction</b>   | <b>3</b>  |
| <b>1.2</b> | <b>General approach of the resolution measurement using photon+jet events</b> | <b>3</b>  |
| <b>1.3</b> | <b>Datasets and event selection</b>   | <b>6</b>  |
| 1.3.1      | Datasets and triggers . . . . .   | 7         |
| 1.3.2      | Simulated samples . . . . .   | 8         |
| 1.3.3      | Event selection . . . . .   | 9         |
| 1.3.3.1    | Jet selection . . . . .   | 9         |
| 1.3.3.2    | Photon selection . . . . .  | 10        |
| 1.3.3.3    | Photon+jet event selection . . . . .  | 11        |
| <b>1.4</b> | <b>Methodology of the measurement</b>   | <b>12</b> |
| 1.4.1      | Validation of the method . . . . .  | 18        |
| <b>1.5</b> | <b>Systematic uncertainties</b>   | <b>20</b> |
| <b>1.6</b> | <b>Results</b>  | <b>25</b> |
| 1.6.1      | Comparison to 2011 measurement . . . . .                                      | 28        |
| 1.6.2      | Comparison to 2012 dijet measurement . . . . .                                | 29        |
| <b>1.7</b> | <b>Discussion and conclusion</b>  | <b>30</b> |
| <b>A</b>   | <b>Measurement of the jet transverse-momentum resolution</b>                  | <b>33</b> |
| A.1        | Pileup reweighting . . . . .  | 33        |
| A.2        | Summary of all selection requirements . . . . .                               | 34        |
| A.3        | Generator-level jet flavor definition . . . . .                               | 34        |
| A.4        | Extrapolation plots . . . . .   | 35        |



24

## **Part 1**

25

**Measurement of the jet**

26

**transverse-momentum resolution**



## 1.1 Introduction

The determination and quantification of the quality of the jet transverse-momentum measurement is of crucial interest for many analyses with jet final states, e. g. the measurement of the dijet cross section [1] or  $t\bar{t}$  production cross sections [2]. Also searches for physics beyond the standard model with missing transverse momentum,  $\cancel{p}_T$ , in the final state rely on a good understanding of  $\cancel{p}_T$  originating from wrongly measured jets [3–5]. It is therefore important to determine the jet transverse-momentum resolution, i. e. the detector resolution of the jet- $p_T$  measurement. For analyses relying on information from simulated data it is necessary to correct the simulated resolution to the resolution actually present in data. Therefore, scale factors will be presented to adjust the resolution in simulation to the resolution of the real detector.

In the following sections, a data-based method to measure the jet- $p_T$  resolution in  $\gamma$ +jet events will be presented. A similar method was already applied in earlier analyses [6,7] of 7 TeV data. It is further developed here and applied to  $19.7\text{ fb}^{-1}$  of  $\sqrt{s} = 8\text{ TeV}$  data.

The method is based on the transverse-momentum balance in the  $\gamma$  + jet system. It takes advantage of the high resolution of the electromagnetic calorimeter and hence the excellent measurement of the photon momentum. Without initial and final state radiation, the photon and the jet are balanced in the transverse plane. Thus, measuring the photon  $p_T$  with high accuracy leads to an accurate estimate of the true jet transverse momentum and offers a possibility to quantify the resolution of jet- $p_T$  measurements.

## 1.2 General approach of the resolution measurement using photon+jet events

The quality of the jet transverse-momentum measurement is determined by the jet transverse-momentum response  $\mathcal{R}$ , i. e. by the ratio of the reconstructed to the true jet transverse momentum

$$\mathcal{R} = \frac{p_{\text{T}}^{\text{reco. jet}}}{p_{\text{T}}^{\text{true jet}}} . \quad (1.2.1)$$

Because of the limited detector resolution, the reconstructed jet  $p_T$  in general differs from the true jet  $p_T$  resulting in a distribution of  $\mathcal{R}$ . In Fig 1.2.1 (left), an exemplary distribution of  $\mathcal{R}$  in simulation (where the true jet  $p_T$  corresponds to the generator-level jet  $p_T$ ) is depicted. The jet transverse-momentum resolution (JER<sup>1</sup>) is defined as the width of the distribution while the mean corresponds to the so-called jet transverse-momentum scale (JES) [8].

It can be seen in Fig. 1.2.1 (left), that the core of the response distribution shows a typical Gaussian behaviour whereas the tails deviate from that functional form. Physical reasons for the pronounced low response tail are, inter alia, semi-leptonic decays of heavy quarks (c- and b-quarks) where the neutrino cannot be detected and the reconstructed transverse momentum of the jet is too small. This effect is visible in Fig. 1.2.1 (right) which depicts the response distribution including all jet flavours (blue), as well as the contribution by c- and b-quarks (red), which is the main contribution to the pronounced left tail. Some instrumental effects, such as a non-linear response of the calorimeter, inhomogeneities of the detector material and electronic noise can contribute to both tails, others, like dead calorimeter channels only contribute to the left tail [9].

In order to avoid the coverage of non-Gaussian tails, the resolution is determined using only the core of the response distribution. The resolution is thus defined as the standard

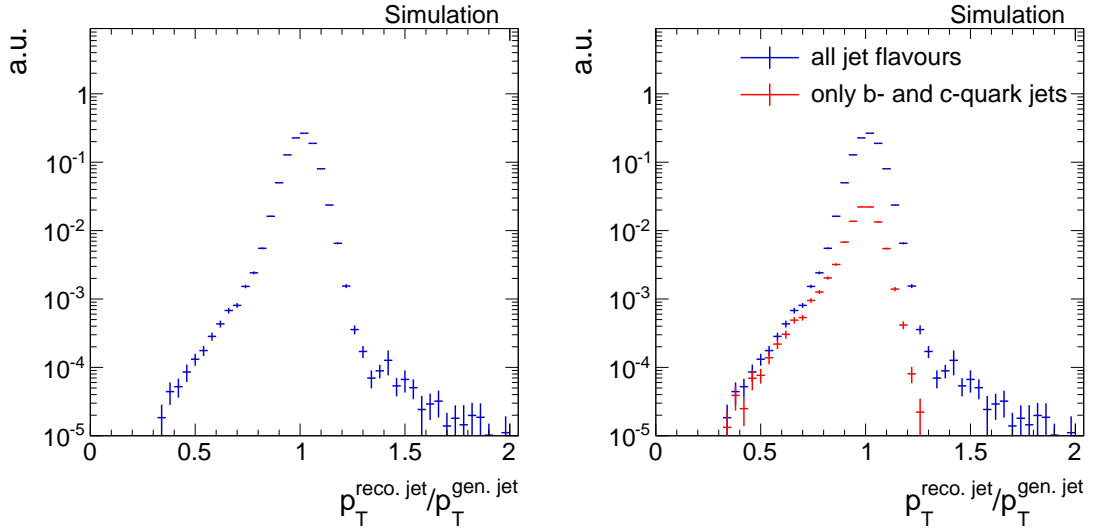


Figure 1.2.1: Left: Normalised number of events over  $p_T^{\text{reco. jet}}/p_T^{\text{gen. jet}}$  from a simulated  $\gamma + \text{jet}$  sample. Right: The response distribution containing all jet flavours (blue) and the contribution by c- and b-quark jets (red).

<sup>1</sup>This abbreviation is a historical relic from experiments where the momentum of jets were only measured in the calorimeters and therefore JER referred to jet energy resolution.

deviation of the 99% truncated response histogram divided by the mean:

$$\sigma_{\text{JER}} = \frac{\sigma_{99\%}}{\mu_{99\%}}.$$

The division by the mean aims at making the resolution independent of the absolute scale (= mean) of the response distribution. It is done because response distributions with a scale smaller than one are typically narrower while distributions with scales larger than one are broader. However, since the scale is very close to one, this is only a tiny effect.

The determination of the 99% range of the histogram is done in several steps. First the mean of the core is found via a Gaussian fit to the histogram in a  $2\sigma$  range<sup>2</sup>. This procedure is done in three iteration steps. Then, a symmetric interval around this mean is determined with its integral equal to 99% of the integral of the full histogram.

As noted earlier, in simulated data, the response distribution can be evaluated by the reconstructed over generator-level jet transverse momentum. A determination of the resolution in real data, however, has to rely on a different approach.

The main idea of a resolution measurement using  $\gamma$ +jet events is based on the transverse-momentum balance of the  $\gamma$  + jet system and the excellent electromagnetic calorimeter resolution.

In Fig 1.2.2, all tree-level processes contributing to an event topology with one photon and one jet in the final state are depicted. Due to momentum conservation, the jet and the photon are back to back in the transverse plane, and therefore,  $\vec{p}_T^\gamma = -\vec{p}_T^{\text{jet}}$ . Because of the high resolution of the electromagnetic calorimeter, photon energies can be measured very accurately (with an resolution between 1.4% and 3.8% in the barrel region for  $\sqrt{s} = 8 \text{ TeV}$  data [10]). Thus, they can serve as an excellent estimator for the true jet transverse-momentum.

Unfortunately, such clean events are very rare processes, and usually, the momentum balance is spoiled by further jet activity from initial and final state radiation (see Fig. 1.2.3). In order to select events that are balanced to a large extent, a lower bound on the angular distance in the transverse plane between the photon and the jet with the

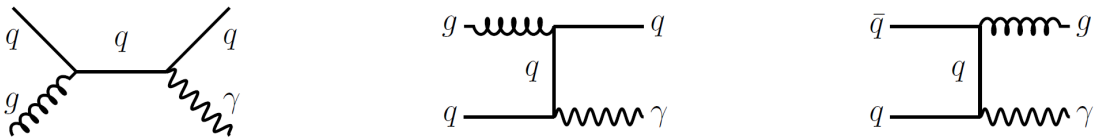


Figure 1.2.2: Tree-level Feynman diagrams of processes in  $pp$ -collisions with one photon and one jet in the final state.

<sup>2</sup>The  $2\sigma$  range is defined as the range  $[\mu - 2\sigma, \mu + 2\sigma]$ .

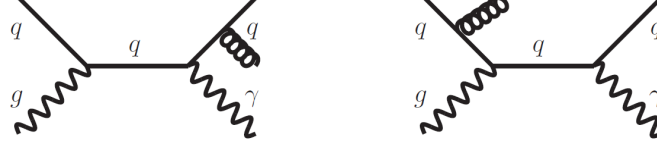


Figure 1.2.3: Tree-level Feynman diagrams with final (left) and initial (right) state radiation.

highest transverse momentum (leading jet) is required:  $\Delta\Phi(1^{\text{st}} \text{ jet}, \gamma) > 2.95 \text{ rad.}$

Additionally, the variable

$$\alpha \doteq \frac{p_{\text{T}}^{2^{\text{nd}} \text{ reco. jet}}}{p_{\text{T}}^{\gamma}}$$

is defined as a measure of further jet activity in an event. It is, however, not sufficient to require only an upper bound on  $\alpha$ . Instead, the jet transverse-momentum resolution is measured in bins of  $\alpha$  with  $\max(\alpha) = 0.2$ , and the extrapolated value to zero further jet momentum at  $\alpha = 0$  is taken as the measured resolution of the jet  $p_{\text{T}}$ .

More formally, measuring the transverse momentum of the photon instead of taking the generator-level jet  $p_{\text{T}}$  leads to the fact that the measured resolution consists of two parts

$$\underbrace{\frac{p_{\text{T}}^{\text{reco. jet}}}{p_{\text{T}}^{\gamma}}}_{\text{measured}} = \underbrace{\frac{p_{\text{T}}^{\text{reco. jet}}}{p_{\text{T}}^{\text{gen. jet}}}}_{\text{intrinsic}} \oplus \underbrace{\frac{p_{\text{T}}^{\text{gen. jet}}}{p_{\text{T}}^{\gamma}}}_{\text{imbalance}}.$$

The intrinsic part is the resolution of interest which is independent of further jets in the event, whereas the imbalance is an artifact of further jet activity and is strongly dependent on  $\alpha$ .

To account for differences in the jet transverse-momentum resolution for different true jet  $p_{\text{T}}$  and different jet pseudorapidity regions, the measurement of the resolution is done in  $p_{\text{T}}^{\gamma}$  bins and bins of  $|\eta|$  of the leading jet.

As noted before, the resolution measurement is important to correct the resolution measured in simulation to the resolution measured in data. Therefore, the measurement of the jet transverse-momentum resolution is conducted on real and on simulated events and data-to-simulation resolution scale factors ( $\rho_{\text{res}}$ ) are determined



## 1.3 Datasets and event selection

The measurement of the jet transverse-momentum resolution is carried out with  $\gamma + \text{jet}$  data recorded during the year 2012 at a centre-of-mass energy of  $\sqrt{s} = 8 \text{ TeV}$  at the CMS experiment. The datasets and triggers that are exploited for this measurement are introduced in the following Section 1.3.1. The measured resolution in data is compared to the resolution in simulated samples. These are introduced in Section 1.3.2. In order to select  $\gamma + \text{jet}$  events that are well suited for the resolution measurement, an event selection is applied on top. This event selection is described in Section 1.3.3.

### 1.3.1 Datasets and triggers

This analysis exploits several triggers which were active during the year 2012 at the CMS experiment. Because of the high production cross section of  $\gamma + \text{jet}$  events, especially for low photon  $p_T$ , almost all of these triggers were highly prescaled, i.e. only a fraction of events were actually recorded when the triggers fired. All triggers that are utilised in this measurement are listed in Table 1.3.1 together with their recorded luminosity. On level one (L1), the triggers rely on single-photon triggers, such as L1SingleEG12 and

Table 1.3.1: Single-photon triggers together with the recorded luminosity taking the prescales of the triggers into consideration.

| Trigger                    | Integrated luminosity [ fb <sup>-1</sup> ] |
|----------------------------|--|
| HLT_Photon30_CaloIdVL_IsoL | 0.0029                                     |
| HLT_Photon50_CaloIdVL_IsoL | 0.0607                                     |
| HLT_Photon75_CaloIdVL_IsoL | 0.123                                      |
| HLT_Photon90_CaloIdVL_IsoL | 0.373                                      |
| HLT_Photon135              | 13.77                                      |
| HLT_Photon150              | 19.71                                      |

130 L1SingleEG30. The L1 triggers require at least one photon that is above a certain  $p_T$   
 131 threshold, e. g. 12 GeV or 30 GeV. The high-level triggers require a photon with a certain  
 132  $p_T$  (as indicated in the name) and, in case of thresholds below 135 GeV, additional quality  
 133 and isolation criteria. All triggers with threshold below 150 GeV were prescaled.

134 The events that are selected by the above mentioned triggers are contained in the  
 datasets listed in Table 1.3.2.

Table 1.3.2: Single-photon data samples used for the resolution measurement with the  
 contained integrated luminosity.

| Dataset                                       | Integrated luminosity [ $\text{fb}^{-1}$ ] |
|---|--|
| /Photon/Run2012A-22Jan2013-v1/AOD             | 0.876                                      |
| /SinglePhoton/Run2012B-22Jan2013-v1/AOD       | 4.412                                      |
| /SinglePhoton/Run2012C-22Jan2013-v1/AOD       | 7.055                                      |
| /SinglePhotonParked/Run2012D-22Jan2013-v1/AOD | 7.354                                      |

135

### 136 1.3.2 Simulated samples

137 In order to compare the measured resolution in data to the resolution in simulation, a  
 138 single-photon sample simulated with PYTHIA6 is used. This sample is generated flat in  
 139 the photon  $p_T$  to have a good statistical precision also for the high photon  $p_T$  region. In  
 140 order to recover a physical  $p_T$  spectrum, all simulated events are reweighted. Figure 1.3.1  
 141 shows the photon  $p_T$  spectrum in simulation before and after the reweighting.

142 All simulated samples come with a pileup scenario which does not necessarily match  
 143 the pileup scenario in data. To match the measured distribution of primary vertices, the  
 144 events are weighted according to their number of primary vertices. Because almost all of  
 145 the used triggers were differently prescaled over time, the distributions of primary vertices  
 146 differ among the sets of events recorded by each trigger. Thus, the reweighting has to be  
 147 done separately for each trigger. A comparison between the number of primary vertices  
 148 in real data and simulation for all triggers can be found in Appendix A.1.

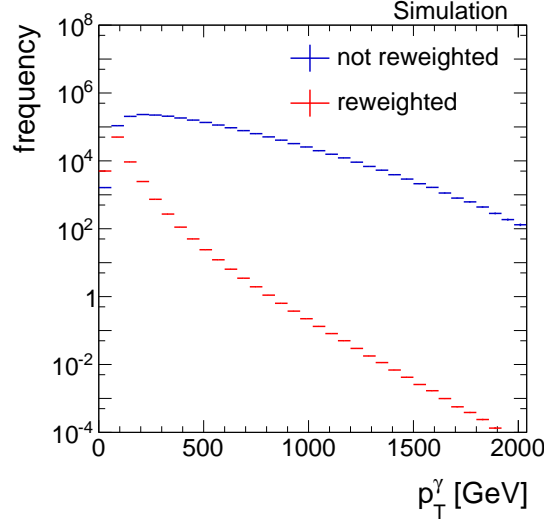


Figure 1.3.1: The photon  $p_T$  spectrum of the PYTHIA6 simulated single-photon sample before (blue) and after (red) reweighting.

### 1.3.3 Event selection

Events are reconstructed with the particle-flow reconstruction algorithm, which uses information of all detector components to reconstruct individual particles [11]. In the following, the selection of well reconstructed jets and photons will be explained as well as the event selection of  $\gamma + \text{jet}$  events.

#### 1.3.3.1 Jet selection

Particles belonging to a jet are clustered with the Anti- $k_t$  jet clustering algorithm with a radius of  $R=0.5$  [12]. Furthermore, all reconstructed jets undergo a so-called “charged hadron subtraction” (CHS) which removes hadrons that are likely caused by pileup events.

To select clean  $\gamma + \text{jet}$  events, it is required that the leading jet meets the “tight ID” selection requirements for jets [13,14]. The tight ID selection ensures a selection efficiency of around 99% and a noise rejection efficiency of 99.98% [13]. It comprises the following selection criteria:

- Neutral hadron fraction  $< 0.90$
- Neutral electromagnetic fraction  $< 0.90$
- Number of constituents  $> 1$

And for jets in the pseudorapidity range  $|\eta| < 2.4$  :

- Charged hadron fraction  $> 0$

- Charged hadron multiplicity  $> 0$
- Charged electromagnetic fraction  $< 0.99$ .

To mitigate effects from pileup, an additional transverse-momentum requirement is imposed:

- $p_T^{1^{\text{st}} \text{ jet}}, p_T^{2^{\text{nd}} \text{ jet}} > 10 \text{ GeV}$ .

### 1.3.3.2 Photon selection

Concerning the photon, a maximum pseudorapidity of the photon of  $|\eta^\gamma| < 1.3$  is demanded to exploit the high resolution of the ECAL in the barrel region.

Furthermore, the resolution is determined for different ranges in photon  $p_T$  to avoid mixing of different prescales of the various triggers. In Table 1.3.3 the applied binning is shown with the respective triggers contributing to each  $p_T^\gamma$  bin.

Table 1.3.3: Photon  $p_T$  bins and corresponding triggers.

| $p_T^\gamma$ -bins | Trigger                       |
|--------------------|-------------------------------|
| 36-60 GeV          | HLT_Photon30_CaloIdVL_IsoL_v* |
| 60-88 GeV          | HLT_Photon50_CaloIdVL_IsoL_v* |
| 88-105 GeV         | HLT_Photon75_CaloIdVL_IsoL_v* |
| 105-149 GeV        | HLT_Photon90_CaloIdVL_IsoL_v* |
| 149-165 GeV        | HLT_Photon135_v*              |
| 165- $\infty$ GeV  | HLT_Photon150_v*              |

QCD-multijet events constitute an important background to  $\gamma + \text{jet}$  events: A photon can be faked by a  $\pi^0$  decaying into two close-by photons. Therefore, a very clean selection of the photons is necessary to suppress this background. The following variables are used (see [15] for further explanation of the variables):

- $\frac{H}{E}$  : The ratio of the measured energy in the hadronic calorimeter over the energy measured in the electromagnetic calorimeter. For photons, this is supposed to be very small as they deposit their energy predominantly in the ECAL.
- $\sigma_{i\eta i\eta}$ : The energy weighted spatial width of the photon energy deposition. The electromagnetic shower of a photon has a small lateral size resulting in small  $\sigma_{i\eta i\eta}$

for prompt photons while showers from fake photons, e.g.  $\pi^0 \rightarrow \gamma\gamma$  have a larger lateral size.

- **Jurassic ECAL isolation:** This isolation criterion uses the information of reconstructed hits “RecHits” (coming from the local reconstruction of the digital signals) in a cone around the photon supercluster of  $R=0.4$ . Those are summed up and an upper criterion is identified to discriminate against background which is typically spatially broader.
- **Tower-based HCAL isolation:** The isolation criterion requires the energy deposited in all HCAL towers around the photon in cone of  $R=0.4$  to be small compared to the photon’s energy.
- **Hollow cone track isolation:** Requires absence of high-energetic tracks around the photon.
- **Pixel seed veto:** In order to reduce the background from electrons and positrons, the absence of a pixel-seed in the pixel tracker along the photons trajectory is required.

The upper bounds that are set on these observables can be found in Table 1.3.4.

Table 1.3.4: Upper bounds for all photon isolation criteria in the barrel ( $|\eta^\gamma| < 1.4442$ ).

|                        | Barrel  |
|------------------------|---|
| $\frac{H}{E}$          | $< 0.05$                                      |
| $\sigma_{i\eta i\eta}$ | $< 0.013$                                     |
| ECAL isolation         | $< 4.2 \text{ GeV} + 0.0060 \cdot p_T^\gamma$ |
| HCAL isolation         | $< 2.2 \text{ GeV} + 0.0025 \cdot p_T^\gamma$ |
| Track Isolation        | $< 2.0 \text{ GeV} + 0.0010 \cdot p_T^\gamma$ |
| Pixel seed veto        | yes   |

### 1.3.3.3 Photon+jet event selection

Besides the mentioned requirements concerning the objects’ attributes, two further criteria related to the event topology are crucial for this analysis:

A lower threshold on  $\Delta\Phi$  between the leading jet and the photon and a maximum value for  $\alpha$

- $\Delta\Phi(1^{\text{st}} \text{ jet}, \gamma) > 2.95 \text{ rad}$

- $\alpha = \frac{p_{\text{T}}^{2^{\text{nd}} \text{ jet}}}{p_{\text{T}}^{\gamma}} < 0.20.$

These requirements are important to suppress events with too much further hadronic activity. A summary of all selection criteria can be found in Appendix A.2.

Finally, the leading jet pseudorapidity interval bounds need to be chosen in order to account for resolution differences in different detector regions. This is done according to [9] with the following binning

$$\begin{aligned} |\eta^{1^{\text{st}} \text{ jet}}| &= 0.0 - 0.5 & |\eta^{1^{\text{st}} \text{ jet}}| &= 1.1 - 1.7 \\ |\eta^{1^{\text{st}} \text{ jet}}| &= 0.5 - 1.1 & |\eta^{1^{\text{st}} \text{ jet}}| &= 1.7 - 2.3. \end{aligned}$$

The binning in the  $p_{\text{T}}^{\gamma}$  dimension is chosen according to the trigger thresholds for  $p_{\text{T}}^{\gamma} < 165 \text{ GeV}$  and ensures sufficient statistical precision for  $p_{\text{T}}^{\gamma} > 165 \text{ GeV}$

|   |  |   |
|---|--|---|
| $p_{\text{T}}^{\gamma} = 36 - 60 \text{ GeV}$   | $p_{\text{T}}^{\gamma} = 149 - 165 \text{ GeV}$  | $p_{\text{T}}^{\gamma} = 200 - 300 \text{ GeV}$ |
| $p_{\text{T}}^{\gamma} = 60 - 88 \text{ GeV}$   | $p_{\text{T}}^{\gamma} = 165 - 176 \text{ GeV}$  | $p_{\text{T}}^{\gamma} = 300 - 400 \text{ GeV}$ |
| $p_{\text{T}}^{\gamma} = 88 - 105 \text{ GeV}$  | $p_{\text{T}}^{\gamma} = 176 - 200 \text{ GeV}$  | $p_{\text{T}}^{\gamma} > 400 \text{ GeV}$       |
| $p_{\text{T}}^{\gamma} = 105 - 149 \text{ GeV}$ | $p_{\text{T}}^{\gamma} = 300 - 400 \text{ GeV}.$ |   |

## 1.4 Methodology of the measurement

The basic methodology of measuring the jet transverse-momentum resolution by exploiting the  $p_{\text{T}}$  balance in  $\gamma + \text{jet}$  events and extrapolating the result to small  $\alpha$ , that was already used in earlier analyses [6, 7], is extended in this measurement in order to explicitly account for the influence of the direction of additional jets on the jet transverse-momentum response.

As already described in Chapter 1.2, the idea behind a resolution measurement with  $\gamma + \text{jet}$  events in real data is the usage of the photon  $p_{\text{T}}$  instead of the true jet  $p_{\text{T}}$ . This

226 results in a twofold contribution to the measured response, the intrinsic response and the  
 227 imbalance:

$$\underbrace{\frac{p_T^{\text{reco. jet}}}{p_T^\gamma}}_{\text{measured}} = \underbrace{\frac{p_T^{\text{reco. jet}}}{p_T^{\text{gen. jet}}}}_{\text{intrinsic}} \oplus \underbrace{\frac{p_T^{\text{gen. jet}}}{p_T^\gamma}}_{\text{imbalance}}. \quad (1.4.1)$$

228 Taking the photon  $p_T$  as true jet  $p_T$  estimator instead of the generator-level jet  $p_T$ , and  
 229 thus measuring the response defined as  $p_T^{\text{reco. jet}}/p_T^\gamma$ , results in a different shape of the  
 230 response distribution compared to the intrinsic response (Fig. 1.4.1). The clear difference  
 231 between the intrinsic response and the imbalance is the double peak structure of the latter  
 232 one. The measured response is a convolution of the two contributions, where the double

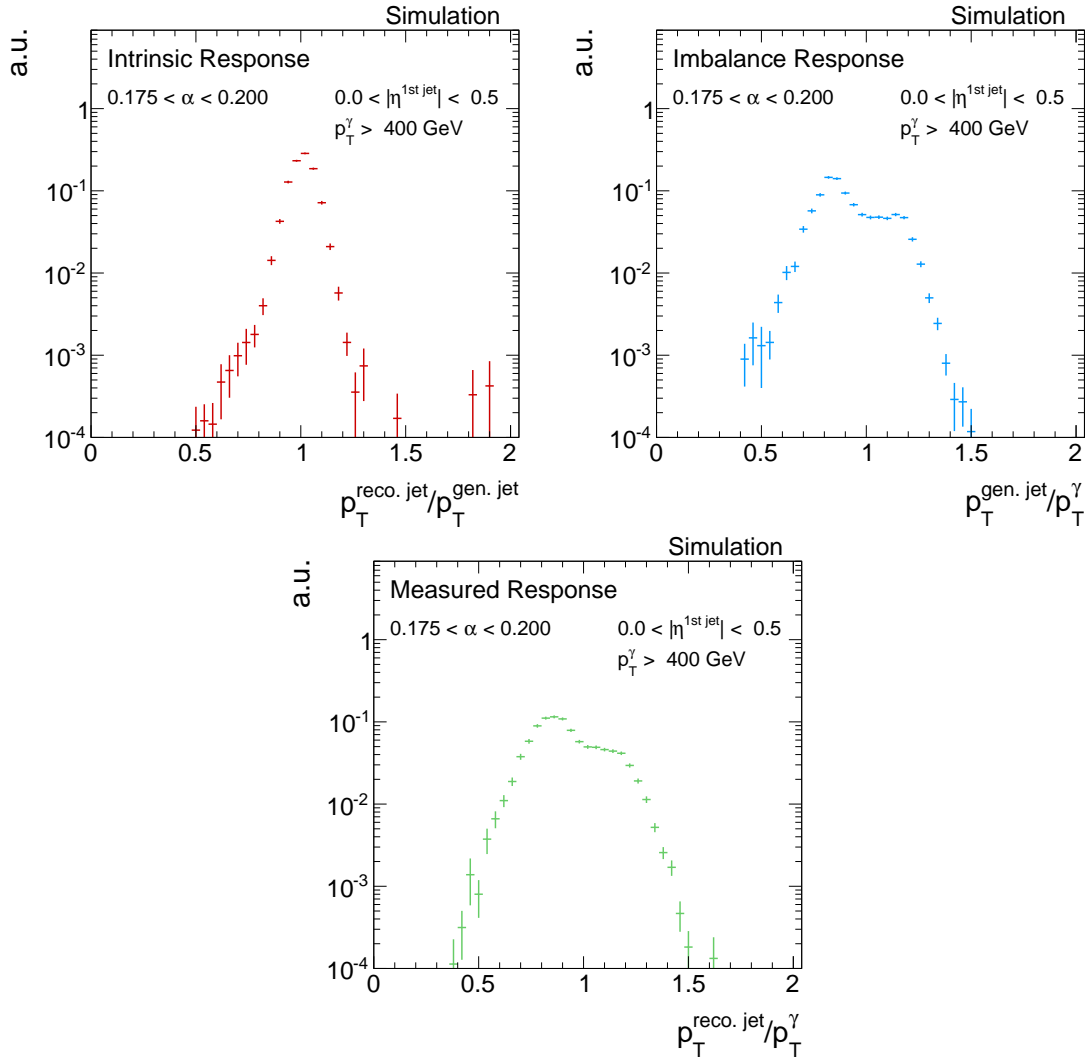


Figure 1.4.1: The two different contributions, intrinsic (top left) and imbalance (top right), to the measured response (bottom) (cf. Eq. (1.4.1)) in simulated events.

233 peak is consequentially less pronounced.

234 The occurrence of two peaks is caused by the hard selection in  $\Delta\Phi$  which forces the  
 235 second jet to be either close to the photon or close to the leading jet due to  $p_T$  conserva-  
 236 tion. An energetic second jet perpendicular to the leading jet-photon axis would require a  
 237 balancing third jet for  $p_T$  conservation. This is very unlikely due to the decreasing proba-  
 238 bility of high jet multiplicities in QCD-multijet events. Events can thus be distinguished  
 239 by the relative direction of the second jet (see Fig. 1.4.2 for a schematic sketch), with a  
 240 hemisphere definition of

$$\begin{aligned} \text{Second jet in 1}^{\text{st}} \text{ jet hemisphere:} \quad & \Delta\Phi(1^{\text{st}} \text{ jet}, 2^{\text{nd}} \text{ jet}) < \Delta\Phi(\gamma, 2^{\text{nd}} \text{ jet}), \\ \text{Second jet in photon hemisphere:} \quad & \text{else.} \end{aligned} \quad (1.4.2)$$

241

242 As can be seen in Fig. 1.4.3, events containing a second jet in the leading jet hemisphere  
 243 lead to a response histogram with mean smaller one, while events with a second jet in  
 244 photon direction result in a distribution with mean larger one. The former occurs more  
 245 frequently because it contains jets from final and initial state radiation, while the latter  
 246 mainly consists only from initial state radiation.

247 The two response distributions coming from the different event topologies are separately  
 248 evaluated. First, the resolution is determined for each of the configurations (cf. Fig. 1.4.3),  
 249 and then, the weighted mean of the two contributions is calculated.

250

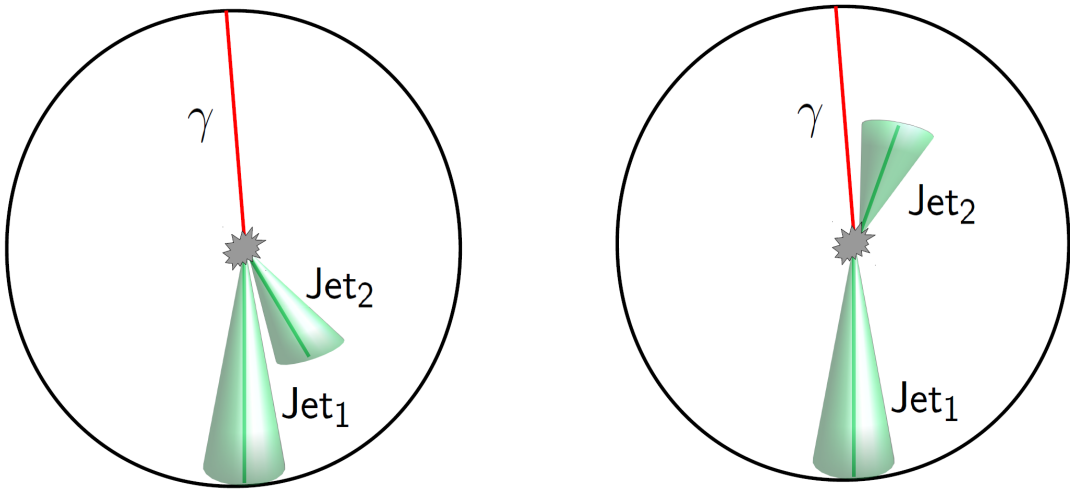


Figure 1.4.2: A schematic sketch of the two different event topologies where the second jet is in the leading jet (left) or the photon hemisphere (right)



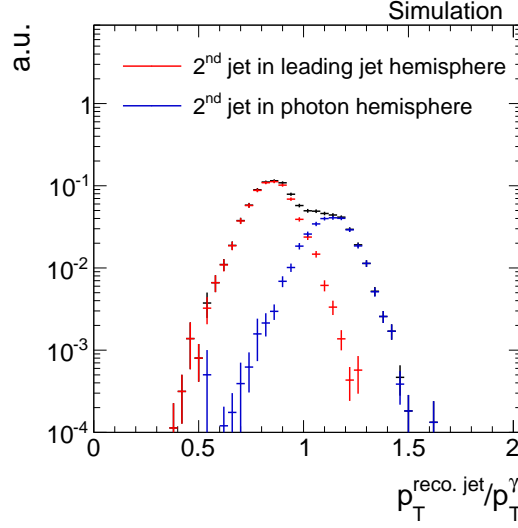


Figure 1.4.3: The measured response with the two contributions visualised. Events with a second jet in photon hemisphere (red) lead to a mean response larger one, while events with a second jet in the leading jet hemisphere (green) have a mean smaller one.

With the above presented methodology, it is possible to measure the resolution in simulation and data for different values of  $\alpha$ . Since the quantity of interest is the jet transverse-momentum resolution independent of further jet activity, i.e. the extrapolated value of the measured resolution at  $\alpha = 0$ , the dependency of the measured resolution on alpha,  $\sigma_{\text{measured}}(\alpha)$ , is needed. Simulated data offers the possibility to study the individual contributions to the measured resolution, the intrinsic resolution  $\sigma_{\text{intrinsic}}(\alpha)$  and the imbalance  $\sigma_{\text{imbalance}}(\alpha)$ .

The intrinsic part of the resolution for a given photon  $p_T$  bin is, by definition, independent of secondary jet  $p_T$ , and can be considered as constant in terms of  $\alpha$

$$\sigma_{\text{intrinsic}}(\alpha) = c. \quad (1.4.3)$$

This is not true for the imbalance part. It was found empirically that the  $\alpha$  dependence of the imbalance can be described by a linear function [7]

$$\sigma_{\text{imbalance}}(\alpha) = q + m \cdot \alpha \quad (1.4.4)$$

Folding two independent Gaussian functions results in a quadratic addition of the corresponding standard deviations  $\sigma_{\text{intr.}} \oplus \sigma_{\text{imb.}}$  and finally yields the functional expression for the measured resolution

$$\sigma_{\text{measured}}(\alpha) = \sqrt{c^2 + q^2 + 2qm \cdot \alpha + m^2 \cdot \alpha^2}. \quad (1.4.5)$$

In Fig. 1.4.4, the  $\alpha$  dependence of the intrinsic resolution (red dots), the imbalance (blue dots), and the measured resolution (green dots) is shown for two exemplary  $p_T^\gamma$  regions in simulated events. The intrinsic resolution is fitted with Eq. (1.4.3) (red line), while the imbalance is fitted with Eq. (1.4.4) (blue line).

It is apparent that the imbalance is not zero for  $\alpha = 0$ . This has two reasons. First and most important, only the photon and the parton are balanced in the transverse plane. But since the transverse momentum of a jet is defined as the sum of all particles' transverse momenta that are clustered into the jet cone, the jet  $p_T$  can be lower than the  $p_T$  of the original parton. This effect is called out-of-cone showering and leads to a residual imbalance between the photon  $p_T$  and the generator-level jet  $p_T$  at  $\alpha = 0$  (parameter  $q$  in Eq. (1.4.4)). Second, the photon  $p_T$  can be wrongly measured and spoil the residual imbalance  $q$ .

Due to the existence of a residual imbalance  $q$ , it is not possible to simply use the measured resolution at  $\alpha = 0$  as an estimator of the intrinsic resolution  $c$ . This is already obvious from Eq. (1.4.5) which evaluates to  $\sigma_{\text{measured}} = \sqrt{c^2 + q^2}$  at  $\alpha = 0$ .

For the determination of the intrinsic resolution in data, the method relies on the residual imbalance information from simulation. Practically, when fitting the measured resolution (Eq.(1.4.5)) in real data, the residual imbalance  $q$  is fixed to the value obtained from the imbalance fit (Eq 1.4.4) in simulation. The intrinsic resolution in real data can then be obtained by extracting the fit parameter  $c$ .

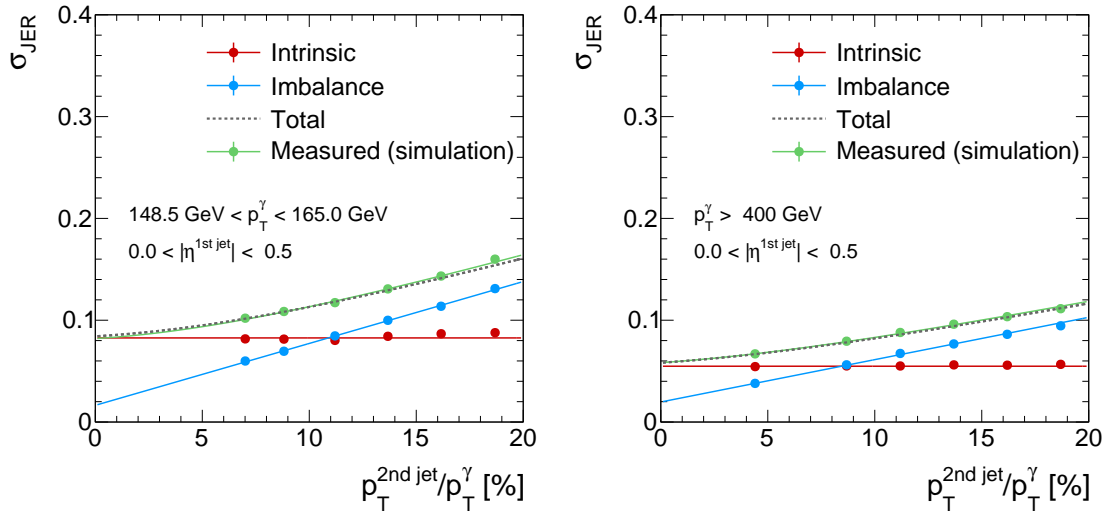


Figure 1.4.4: The alpha dependency of the various parts of the resolution in the simulated events for  $83 \text{ GeV} < p_T^\gamma < 99 \text{ GeV}$  (left) and  $400 \text{ GeV} < p_T^\gamma$  (right). The total resolution (grey dotted line) is the addition in quadrature of the imbalance (blue line) and the intrinsic (red line) fit functions. It can be compared to the measured pseudo data (green dots/line).

For consistency, the same approach is used for simulated data. The fitted function of the measured resolution (green line) in Fig. 1.4.4 corresponds to the fit function of Eq. (1.4.5) with the parameter  $q$  fixed to the value obtained from the imbalance fit (blue line). Finally, the dotted grey line is the total resolution with the analytic expression of function (1.4.5) with the parameters set to the fit values of the intrinsic (red) and the imbalance fit (blue). It can be nicely seen that the total resolution and the fit function of the measured resolution (green line) are well in agreement. This implies, that the assumed functional forms of the resolution components and the assumed convolution leads indeed to a good description of the measured resolution. Further validations of the methodology will be described in Section 1.4.1.

In Fig. 1.4.5, the extracted intrinsic resolution in simulation (green) and real data (black) is shown in the different photon  $p_T$  bins for two different  $|\eta^{1\text{st jet}}|$  regions. The resolution improves for increasing photon  $p_T$ . For the  $|\eta^{1\text{st jet}}| < 0.5$  region, the resolution is approximately 10% for  $p_T^\gamma \approx 100$  GeV and decreases to values around 6% for  $p_T^\gamma \approx 500$  GeV. The increasing statistical uncertainties for low photon  $p_T$  arise through the requirement of a maximal  $\alpha$  and a minimal  $p_T$  of the second jet. This reduces the numbers of events in the low photon  $p_T$  bins. For events with  $p_T^\gamma \lesssim 50$  GeV, it is not possible at all to fulfil both requirements at the same time.

From Fig. 1.4.5, it can be seen that the resolution in data is always worse than the resolution in simulation. Thus, in order to measure data-to-simulation scale factors  $\rho_{\text{res}}$  for the jet transverse-momentum resolution, the measured resolution in data is divided by

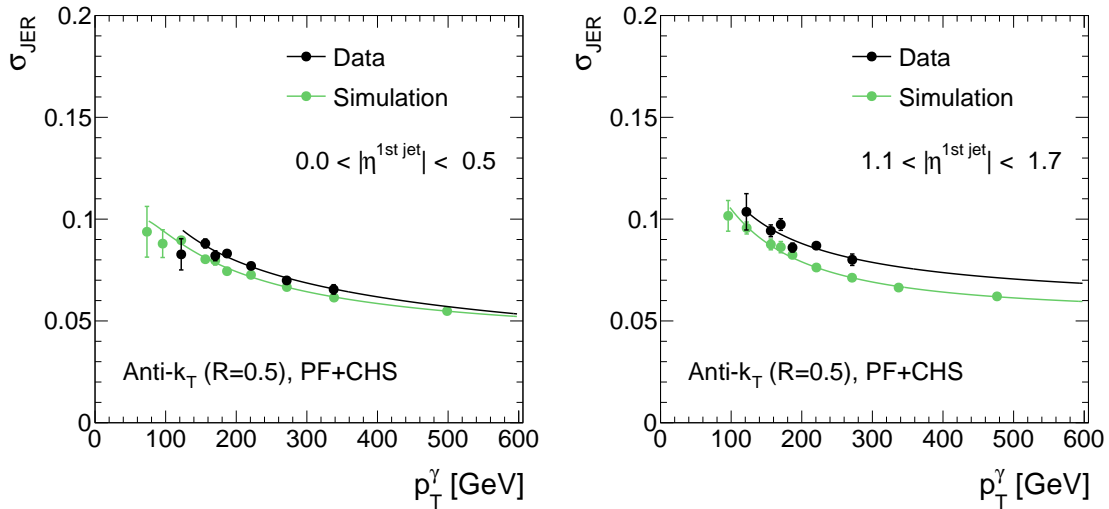


Figure 1.4.5: Resolution for  $|\eta^{1\text{st jet}}| < 0.5$  (left) and  $1.1 < |\eta^{1\text{st jet}}| < 1.7$  (right) in simulation (green) and real data (black). Both are fitted with a particle-flow resolution function introduced in [6].

the resolution in Monte Carlo simulation (MC).

$$\rho_{\text{res}} = \frac{\sigma_{\text{JER}}^{\text{data}}}{\sigma_{\text{JER}}^{\text{MC}}} \quad (1.4.6)$$

The results will show (Chapter 1.6), that this ratio is independent of the  $p_{\text{T}}^{\gamma}$  and can thus be fitted with a constant in terms of  $p_{\text{T}}^{\gamma}$ . The measurement of the data-to-simulation scale factors is therefore only done in bins of  $|\eta^{1^{\text{st}} \text{ jet}}|$ .

How to apply these scale factors and adjust the jet transverse-momentum resolution in simulation to the measured resolution in data is well described in [9].

### 1.4.1 Validation of the method

The method is validated with simulated events. The bias of the method is shown in Fig. 1.4.6 for the barrel region. It is evaluated as the ratio of the predicted intrinsic resolution by fitting Eq. (1.4.5) with  $q$  fixed to the value obtained by Eq. (1.4.4) over the intrinsic resolution directly obtained from the intrinsic response distribution  $p_{\text{T}}^{\text{reco. jet}}/p_{\text{T}}^{\text{gen. jet}}$ . The result is in good agreement with the expectation to better than 5% above 100 GeV and better than 1% above 200 GeV. Only for small  $p_{\text{T}}$ , larger deviations are observed, which are systematically lower than zero (up to 15%).

The residual bias of the method for small  $p_{\text{T}}^{\gamma}$  is stemming from two effects: First, the binning in  $p_{\text{T}}^{\gamma}$  and the momentum balance between the photon and the first two jets lead

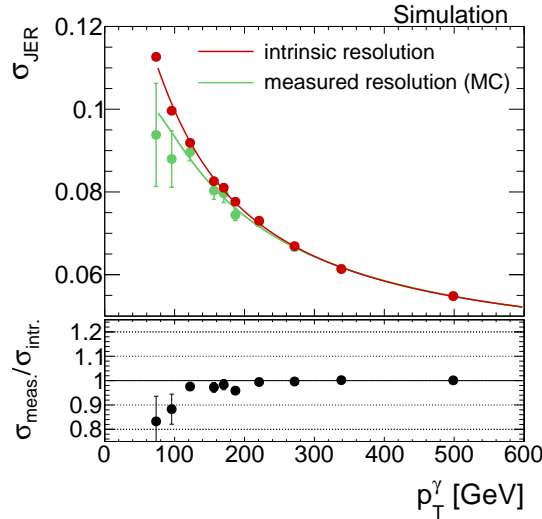


Figure 1.4.6: Consistency check of the method: Comparison between the “measured” resolution evaluated with Eq. (1.4.5) and the intrinsic resolution from Eq. (1.4.3) in simulation.

to a dependency of the first jet  $p_T$  on the second jet  $p_T$  and therefore alpha: For a fixed  $p_T^\gamma$ , the  $p_T$  of the first jet gets smaller for larger  $p_T^{2^{\text{nd}} \text{ jet}}$  in events where the second jet is in the leading jet hemisphere (see Fig. 1.4.2), leading to a dependency of  $p_T^{1^{\text{st}} \text{ jet}} \propto -p_T^{2^{\text{nd}} \text{ jet}}$ . This effect is directly opposite for events with a second jet in the photon hemisphere. In these events, the first jet  $p_T$  gets larger for larger  $p_T^{2^{\text{nd}} \text{ jet}}$  and thus  $p_T^{1^{\text{st}} \text{ jet}} \propto p_T^{2^{\text{nd}} \text{ jet}}$  for fixed  $p_T^\gamma$ . As the resolution of the jet improves with higher jet  $p_T$  (see Fig. 1.4.5), a dependency of the leading jet  $p_T$  on the second jet  $p_T$  directly leads to a dependency of the intrinsic resolution on the second jet  $p_T$ . In principle, as the effect is opposite for events in the different hemispheres, it should cancel out, when taking the weighted mean of the two hemisphere resolutions. But as the topology of a second jet in the leading jet hemisphere is much more frequent, a residual upward trend in the intrinsic resolution vs.  $\alpha$  is conserved.

The second source of the residual bias arises from the alpha definition  $\alpha = p_T^{2^{\text{nd}} \text{ jet}}/p_T^\gamma$ . Because of the inclusion of  $p_T^\gamma$  in  $\alpha$  with  $\alpha \propto 1/p_T^\gamma$ , the high photon  $p_T$  events accumulate in the low alpha regions. As the selected events are almost balanced, a high  $p_T^\gamma$  is associated with a high jet  $p_T$ , thus also the high jet  $p_T$  events accumulate in the low alpha bins, leading to an upward trend in the intrinsic resolution vs.  $\alpha$ . This behaviour can be seen in the intrinsic resolution in Fig. 1.4.4, where a small increase of the resolution to high  $\alpha$  can be seen. By fitting a horizontal line to the intrinsic resolution, this effect is averaged out. But the measured resolution with an additional free parameter can adopt this increase and result, therefore, in a y-intercept which is too small. For high photon  $p_T$  bins, this effect is less pronounced, as the slope of  $\text{JER}(p_T^\gamma)$  (see Fig. 1.4.4) flattens out.

However, this is not of concern here, because the results of the measurement will be presented as resolution scale factors ( $\rho_{\text{res}}$ ), defined as the resolution measured in data divided by the resolution measured in Monte Carlo simulation (see Eq. (1.4.6)). Hence, a possible bias in the separate resolution measurements for data and simulation should cancel out. To prove this hypothesis, the simulated dataset is smeared with input values  $\rho_{\text{res}} = 1.1$  in all  $|\eta^{1^{\text{st}} \text{ jet}}|$  bins. As done to determine the data-to-simulation ratio, the relative difference of the resolution measured in the smeared and in the non-smeared dataset is fitted with a constant over the photon  $p_T$  range. The resulting scale factors  $\rho_{\text{res}}$  should reproduce the input value of  $\rho_{\text{res}} = 1.1$ .

In Fig. 1.4.7, the comparison of the input and output values is shown. In all  $|\eta^{1^{\text{st}} \text{ jet}}|$  bins, the measurement of the scale factors reproduces the input factors within the statistical uncertainties. The deviation of the measured scale factors to the input value is less than 0.9% in all four  $|\eta^{1^{\text{st}} \text{ jet}}|$  bins. Thus, the method is expected to hold also for the determination of the data-to-simulation ratio.

After the characterisation and estimation of the associated systematic uncertainties of

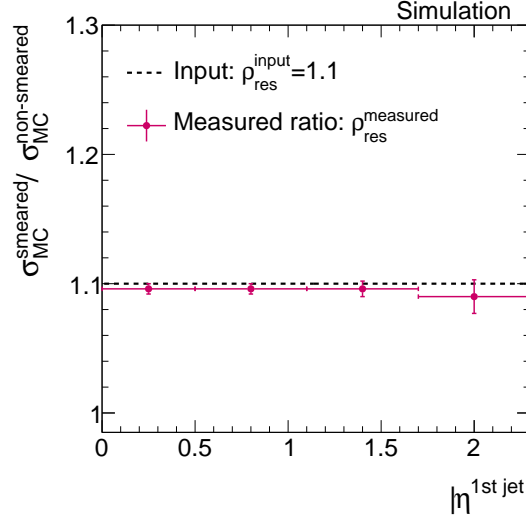


Figure 1.4.7: Comparison of the resolution ratio  $\sigma_{\text{JER}}^{\text{smeared MC}} / \sigma_{\text{JER}}^{\text{non-smeared MC}}$  measured in simulated events with the input smearing factor  $\rho_{\text{res}} = 1.1$  in all four  $|\eta^{1\text{st jet}}|$  bins.

the jet transverse-momentum resolution measurement with  $\gamma + \text{jet}$  events, the results of the measurement on  $\sqrt{s} = 8 \text{ TeV}$  data will be presented.

## 1.5 Systematic uncertainties

Many systematic uncertainties of the jet transverse-momentum resolution measurement cancel out when focusing on the data-to-simulation ratio  $\sigma_{\text{JER}}^{\text{data}} / \sigma_{\text{JER}}^{\text{MC}}$ . In the following subsections, only uncertainties relevant for this ratio will be discussed.

For the final uncertainty, the single uncertainties are added in quadrature, resulting in relative uncertainties between 2.3% to 6.3% for the lowest and highest  $|\eta^{1\text{st jet}}|$  bin, respectively.

An overview of all systematic uncertainties can be found in Table 1.5.1.

### Uncertainty on the contamination with QCD-multijet events

Although the photon selection is very strict (see Section 1.3.3), due to the huge QCD-multijet cross section, a countable fraction of dijet events can survive the selection with a jet misidentified as photon. This happens, when e. g. a jet hadronises to a  $\pi^0$  that decays

Table 1.5.1: All relative systematic uncertainties on the data-to-simulation ratio  $\sigma_{\text{JER}}^{\text{data}}/\sigma_{\text{JER}}^{\text{MC}}$  listed by sources for the different  $|\eta^{\text{jet}}|$  bins.

|  | $ \eta^{\text{jet}} $ |           |           |           |
|--|-----------------------|-----------|-----------|-----------|
|  | 0.0 - 0.5             | 0.5 - 1.1 | 1.1 - 1.7 | 1.7 - 2.3 |
| <b>Multijet contamination</b>              | +2.0%                 | +2.0%     | +2.3%     | +2.5%     |
|  | -2.0%                 | -2.0%     | -2.3%     | -2.5%     |
| <b>Simulation of flavor composition</b>    | +0.9%                 | +0.9%     | +0.8%     | +0.6%     |
|  | -0.9%                 | -0.9%     | -0.8%     | -0.6%     |
| <b>Simulation of out-of-cone showering</b> | +0.5%                 | +2.8%     | +3.6%     | +5.7%     |
|  | -0.5%                 | -2.8%     | -3.6%     | -5.7%     |
| <b>Jet energy scale</b>                    | +0.6%                 | +0.6%     | +0.6%     | +0.7%     |
|  | -0.5%                 | -0.6%     | -0.6%     | -0.6%     |
| <b>Pileup reweighting</b>                  | +0.1%                 | +0.1%     | +0.1%     | +0.2%     |
|  | -0.1%                 | -0.1%     | -0.2%     | -0.2%     |
| <b>Total</b>                               | +2.3%                 | +3.6%     | +4.4%     | +6.3%     |
|  | -2.3%                 | -3.6%     | -4.4%     | -6.3%     |

to two photons which is sometimes not distinguishable from the isolated photon of a  $\gamma$ +jet event for the detector.

In principle, those dijet events have the same topology as  $\gamma$ +jet events. The two leading jets are also balanced apart from initial and final state radiation. Therefore, the method is generally expected to hold. A worsening of the resolution because of background contamination is only expected due to the mismeasurement of the  $p_{\text{T}}$  of the jet misidentified as photon, because only the energy of the  $\pi^0$  is counted and not the full energy. Another aspect is the different flavor composition of a QCD-multijet sample. Due to the different production mechanism, QCD-dijets are predominantly initiated by gluons while the leading jet in  $\gamma$ +jet events often stems from a light quark, cf. Fig. 1.2.2. The number of particles after hadronisation is typically larger for gluon jets, hence the single particles are less energetic and out-of-cone showering is more pronounced. Since in this analysis the residual imbalance  $q$  is taken from the simulation where only a  $\gamma$ +jet sample is considered, it is not expected to accurately describe the residual imbalance in the data sample where

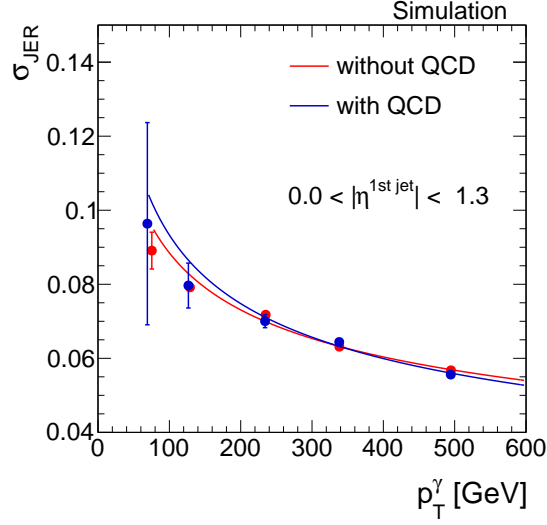


Figure 1.5.1: The jet transverse-momentum resolution measured in simulation for  $|\eta^{1\text{st jet}}| < 1.3$  with (blue) and without (green) a QCD-multijet sample added to the  $\gamma + \text{jet}$  sample.

also dijet events occur.

To investigate the impact of QCD-multijet contamination, a QCD-multijet sample, enriched in jets with a large electromagnetic fraction, is added to the  $\gamma + \text{jet}$  sample and weighted according to the cross section. Since the QCD-multijet sample has very large event weights leading to high statistical uncertainties in the measured jet transverse-momentum resolution, some selection criteria ( $\alpha < 0.4$  and  $\Delta\Phi > 2.7$ ) are relaxed in order to increase the statistical precision of the uncertainty estimation. Additionally, a rougher binning in  $\alpha$ ,  $p_T^\gamma$  and  $|\eta^{1\text{st jet}}|$  is applied.

The residual imbalance  $q$  of the resolution measurement including the QCD-multijet sample is fixed to the residual imbalance determined from the  $\gamma + \text{jet}$  only analysis to account for a possible error in the evaluation of the  $\sigma_{\text{JER}}^{\text{data}}/\sigma_{\text{JER}}^{\text{MC}}$  ratio where data is only compared to a  $\gamma + \text{jet}$  sample.

In Fig. 1.5.1, the resolution measured when using both the  $\gamma + \text{jet}$  and the QCD-multijet sample is compared to the resolution measured only with the  $\gamma + \text{jet}$  sample. It can be seen, that the resolution is worse for low  $p_T^\gamma$  when considering QCD-multijet contamination.

The impact on the data-to-simulation ratio is estimated by adding the QCD-multijet sample on top of the  $\gamma + \text{jet}$  sample and redoing the evaluation of the scale factors. The resulting uncertainties vary between 2.0 – 2.5% for the different  $|\eta^{1\text{st jet}}|$  regions (cf. Table 1.5.1).



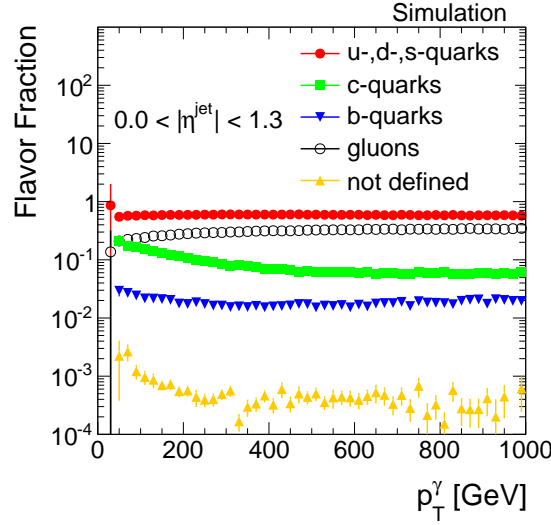


Figure 1.5.2: The flavor composition in the  $\gamma + \text{jet}$  sample in the barrel region of the detector. The “algorithmic” flavor definition is used (see Appendix A.3 for more details).

## Uncertainty on the flavor composition in simulation

A possible difference among the resolution of different jet flavors (caused by e.g. more pronounced out-of-cone showering of gluon jets) should in principle not play a role for the data-to-simulation scale factors  $\rho_{\text{res}}$  as long as the flavor composition of the data and simulation samples is the same.

To account for possible discrepancies in the flavor composition between data and simulation, the gluon and quark flavor fractions of the simulated sample are varied by 10%.

To estimate the effect of different flavour compositions, the resolution in simulation is separately evaluated for quarks ( $\sigma_{\text{JER}}^{\text{quarks}}$ ) and gluons ( $\sigma_{\text{JER}}^{\text{gluons}}$ ). There are various definitions used in the CMS collaboration how to assign the underlying generator-level quark/gluon flavor to a jet. In this measurement the so-called “algorithmic” flavor definition is used which classifies b- or c-jets from gluon splitting as b- or c-quarks (see Appendix A.3 for more details on this definition).

Figure 1.5.3 shows the differences in the resolution for all flavors separately for  $|\eta^{\text{1st jet}}| < 1.3$ . The composition in the simulated PYTHIA  $\gamma + \text{jet}$  sample is around 60% light quarks and 20% to 35% gluons (see Fig. 1.5.2). The missing fraction is mainly made up out of charm quarks.

The resolution for gluon and light quark jets is comparable for small  $p_T^\gamma$  and gets larger for high  $p_T^\gamma$ . Since the transverse momentum of neutrinos is counted into the generator-level jet  $p_T$ , the resolution of charm and bottom quarks is therefore shifted to larger resolution values (left part of Fig. 1.5.3). This is not the case, if the neutrino  $p_T$  is not

added to the generator-level jet  $p_T$ , as can be seen in Fig 1.5.3 (right). However, for the here presented measurement it does not play a role whether the neutrino  $p_T$  is or is not added to the generator-level jet  $p_T$ , because in case it is not included into the intrinsic response the long right tail of the response function for b- and c-quarks is then transferred to the imbalance response. Thus, the right tail of b- and c-quarks does anyway enter the jet transverse-momentum resolution measurement with  $\gamma + \text{jet}$  events, either in the intrinsic or in the imbalance response.

The weighted mean of the quark and the gluon resolution is then taken to estimate the resolution for different flavor compositions, such that the flavor fractions are varied by 10%. Finally, the constant fit to the data-to-simulation ratio  $\sigma_{\text{JER}}^{\text{data}}/\sigma_{\text{JER}}^{\text{MC}}$  is reevaluated, leading to a final systematic uncertainty between 0.6 – 0.9%.

### Uncertainty on the simulation of out-of-cone showering

Another source of uncertainty is the use of information from Monte Carlo simulation by determining the residual imbalance  $q$  from the simulated  $\gamma + \text{jet}$  sample (Eq. (1.4.5)).

Since it cannot be expected that out-of-cone showering is well modelled in simulation, possible differences between real and simulated out-of-cone showering are estimated by the evaluation of the ratio  $\sigma_{\text{JER}}^{\text{data}}/\sigma_{\text{JER}}^{\text{MC}}$  using different jet radii of the jet reconstruction algorithm.

For the primary analysis, jets reconstructed by the Anti- $k_t$  algorithm with a radius of

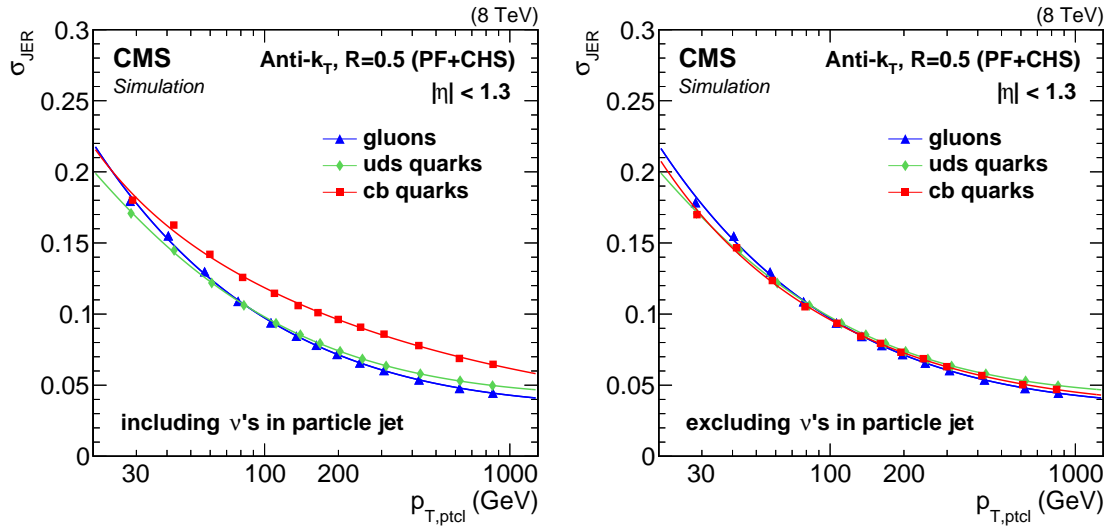


Figure 1.5.3: The intrinsic resolution  $\sigma_{\text{intr.}}$  for  $|\eta^{\text{1st jet}}| < 1.3$  for different jet flavors with (left) and without (right) including the neutrinos in the generator-level jet. Here, JER refers to  $\sigma_{\text{intr.}}$ , and  $p_{T,\text{ptcl}}$  to the generator-level jet  $p_T$ .

$R = 0.5$  are used (AK5-jets). In order to evaluate the systematic uncertainty on the out-of-cone showering simulation, the measurement of  $\rho_{\text{res}}$  redone with jets reconstructed with a jet radius of  $R = 0.7$  (AK7-jets).

The data-to-simulation ratio is in all  $|\eta^{1^{\text{st jet}}}|$  bins larger for AK7-jets, resulting in uncertainties between 0.5 – 5.7%. The uncertainty on the simulation of out-of-cone showering is thereby the largest systematic uncertainty of this measurement.

## Uncertainty on the jet energy scale

A further uncertainty arises from the correction of the jet energy scale. The transverse momentum of each jet is corrected in order to have uniform response over the full  $\eta^{\text{jet}}$ , and  $p_{\text{T}}^{\text{jet}}$  range [8]. In simulation, it is additionally corrected to account for data-simulation differences. The latter correction can be a important for the evaluation of the data-to-simulation ratio  $\rho_{\text{res}}$ . Thus, the uncertainties on the correction factors that are only applied to the simulated samples are varied up and down within their  $1\sigma$ -uncertainties.

The effect of the jet  $p_{\text{T}}$  variation on the data-to-simulation ratio is of minor importance and range between 0.5 – 0.7%.

## Uncertainty on the pileup reweighting

Finally, an uncertainty due to the adjustment of the simulated events to the pileup distribution in data is evaluated.

To account for this uncertainty, the effect of a 5.0% up- and downward variation of the minimum-bias cross section (69.4 mb) on the resolution is evaluated, following the recommended procedure from [?]. The resulting uncertainties are almost negligible and range between 0.1 – 0.2%.

# 1.6 Results

The data-to-simulation resolution scale factors  $\rho_{\text{res}}$  are determined in  $19.7 \text{ fb}^{-1}$  of  $pp$ -collision data at  $\sqrt{s} = 8 \text{ TeV}$  with the methodology described in Chapter 1.4. In each  $\alpha$ -,  $p_{\text{T}}^{\gamma}$ - and  $|\eta^{1^{\text{st jet}}}|$ -bin, the width of the 99% truncated response histogram is determined in simulation and data. Afterwards, the extrapolation to zero additional jet activity is carried out, by fixing the imbalance  $q$  in simulation and in data to the value extracted from the imbalance extrapolation in simulation. Exemplary extrapolations for the imbalance, the intrinsic and the measured resolution in simulation and the measured resolution in

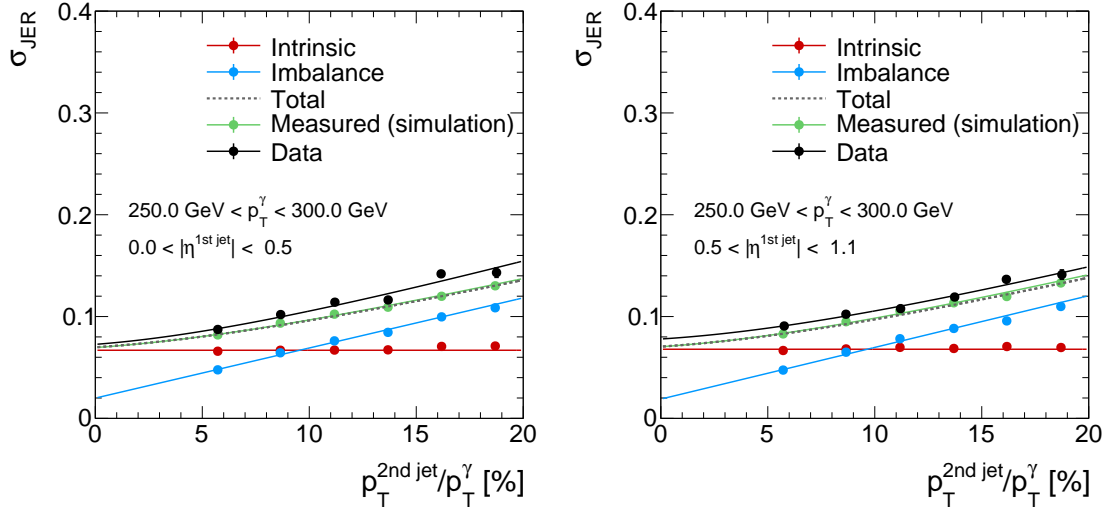


Figure 1.6.1: Two examples of the alpha dependency of the measured jet transverse-momentum resolution in data (black dots), in simulation (green dots) and of the intrinsic (red dots) and the imbalance (blue dots) part of the resolution in simulated events. All resolutions are fitted with the corresponding functions introduced in Chapter 1.4 (Eqs. (1.4.3)- (1.4.5)). The total resolution (grey dotted line) is the addition in quadrature of the imbalance (blue line) and the intrinsic (red line) fit functions.

477 data are shown in Fig. 1.6.1. The full set for each  $p_T^\gamma$  and  $|\eta^{1\text{st jet}}|$  bin can be found in  
 478 Appendix A.4.

479 Finally, the extracted resolutions in data and simulation in every  $p_T^\gamma$  bin are divided  
 480 and a horizontal fit is applied to this ratio

$$\frac{\sigma_{\text{JER}}^{\text{data}}}{\sigma_{\text{JER}}^{\text{MC}}} (p_T^\gamma) .$$

481 In Fig. 1.6.2, the results for all four  $|\eta^{1\text{st jet}}|$ -ranges are depicted. The  $\chi^2/\text{NDF}$ -values for  
 482 the four fits vary between 0.23 and 2.53. Thus, a horizontal fit is justified, and one value  
 483 for every  $|\eta^{1\text{st jet}}|$ -bin will be reported.

484 All fit results are greater than one which means that the resolution in data is in all bins  
 485 worse compared to the resolution in simulation. The values of the fits range from 1.067  
 486 (for the first  $\eta^{\text{jet}}$ -bin) to 1.199 (for the last  $\eta^{\text{jet}}$ -bin).

487 The systematic uncertainties are evaluated as described in the previous chapter. The  
 488 single uncertainties are taken as upper and lower boundary of the 68% uncertainty band  
 489 and are added in quadrature to get the total systematic uncertainty. Table 1.6.1 sum-  
 490 marises the data-to-simulation ratio results determined with data collected during the  
 491 year 2012 with their statistical and systematic uncertainties. The visualised result can

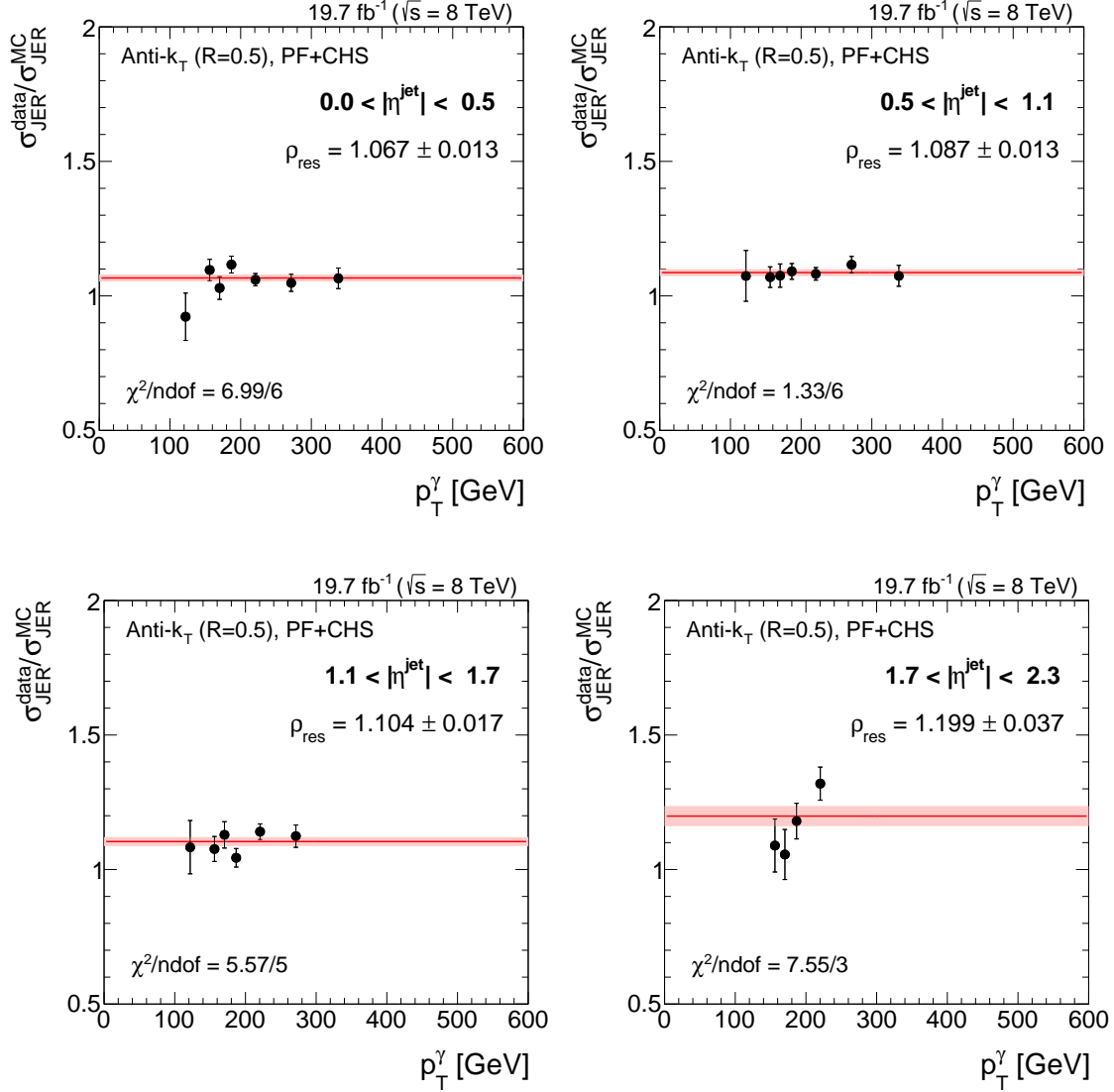


Figure 1.6.2: Data-to-simulation resolution ratios (black dots), fitted with a horizontal line (red line) for four different  $|\eta^{\text{jet}}|$ -ranges. The fit uncertainties are depicted with light red error bands.

be found in Fig. 1.6.3.

Though the  $\gamma + \text{jet}$  analysis is known to be capable to produce highly precise results, the systematic uncertainties are still dominating. This is mainly caused by the uncertainty on the simulation of out-of-cone showering. The statistical limitation of this analysis is due to the collected data at the CMS detector. The number of simulated events is roughly eight times larger.

Table 1.6.1: Data-to-simulation resolution scale factors  $\rho_{\text{res}}$  with statistical and systematic uncertainties.

| $ \eta^{\text{jet}} $ | $\rho_{\text{res}}$ | stat.       | sys.                 |
|-----------------------|---------------------|-------------|----------------------|
| 0.0 – 0.5             | 1.067               | $\pm 0.013$ | $+0.025$<br>$-0.024$ |
| 0.5 – 1.1             | 1.087               | $\pm 0.013$ | $+0.039$<br>$-0.039$ |
| 1.1 – 1.7             | 1.104               | $\pm 0.017$ | $+0.049$<br>$-0.049$ |
| 1.7 – 2.3             | 1.199               | $\pm 0.037$ | $+0.075$<br>$-0.075$ |

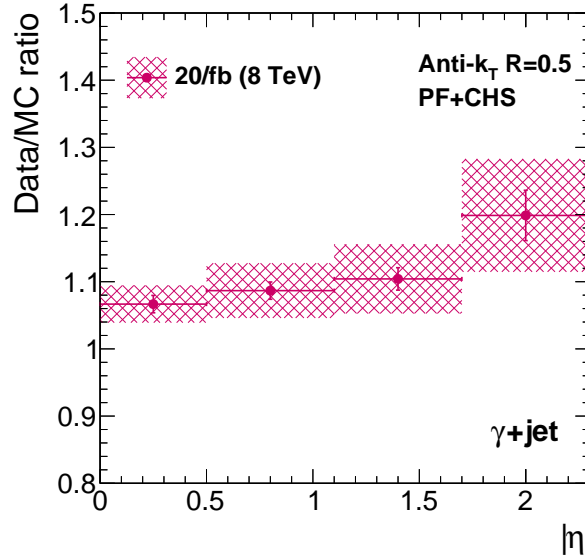


Figure 1.6.3: The measured data-to-simulation resolution ratio in  $\gamma + \text{jet}$  events using data recorded in the year 2012. The red band depicts the total uncertainty whereas the error bars show the statistical uncertainty only.

### 499 1.6.1 Comparison to 2011 measurement

500 A comparison of the data-to-simulation resolution scale factors  $\rho_{\text{res}}$  between this analysis  
501 and the results of 2011 which were determined from a dijet data sample [9] can be found  
502 in Fig. 1.6.4.

503 It can be seen, that throughout the whole  $\eta^{\text{jet}}$ -range the data-to-simulation are system-  
504 atically larger for the result in 2011.

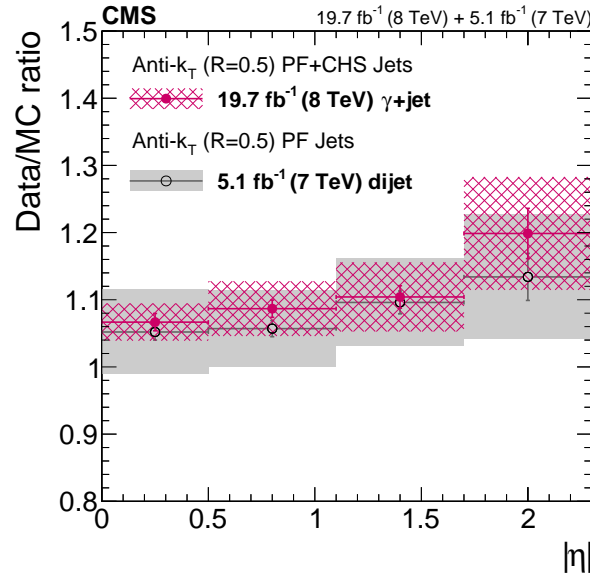


Figure 1.6.4: FIXME (update this plot): Data-to-simulation jet- $p_T$  resolution ratio determined from  $\gamma$  + jet events from 2012 compared to dijet results from 2011. The grey and magenta bands correspond to the full uncertainties, whereas the error bars depict the statistical uncertainties only.

Comparing the precision of both measurements, the  $\gamma$ +jet analysis is for all  $\eta$ -bins more precise than the analysis done with dijet events. This is due to the smaller systematic uncertainties of the  $\gamma$  + jet analysis which compensates for the better statistical precision of the QCD-multijet sample due to the large cross section.

## 1.6.2 Comparison to 2012 dijet measurement

In 2012, also a jet- $p_T$  resolution measurement was conducted with the help of dijet events [8, 16]. A comparison of the here presented measurement using  $\gamma$  + jet events to the measurement with dijet events can be found in Fig. 1.6.5. Both measurements are compatible within their uncertainties. It can be seen that the statistical precision is much better for the measurement with QCD-multijet events because of the larger cross section. The systematic uncertainties are of comparable size for small pseudorapidity bins and are larger for high  $|\eta^{\text{jet}}|$  in the  $\gamma$  + jet measurement. This is due to the uncertainty on the simulation of the out-of-cone showering. This uncertainty plays a smaller role in the dijet measurement (between 0.4% and 1.5%) as the effect by out-of-cone showering partly cancels out in case of two balanced jets.

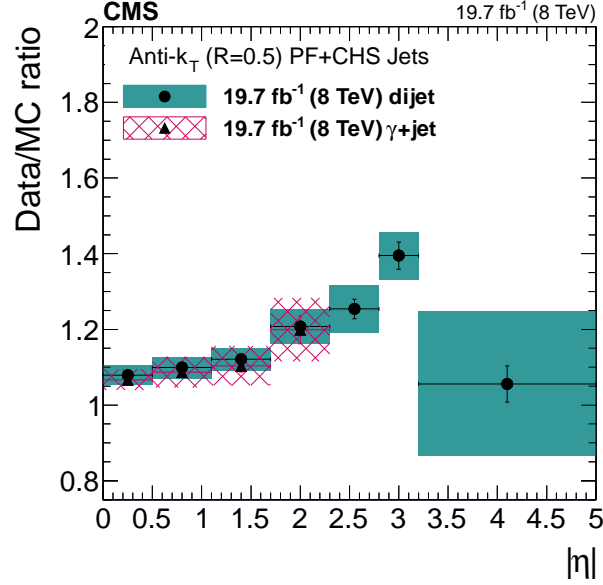


Figure 1.6.5: FIXME: Data-to-simulation jet- $p_T$  resolution ratio determined from  $\gamma + \text{jet}$  events from 2012 compared to dijet results from 2012. The blue and magenta bands correspond to the full uncertainties, whereas the error bars depict the statistical uncertainties only.

## 1.7 Discussion and conclusion

The difference between data and simulation of the jet-transverse momentum resolution is an important input for many analyses at CMS, among them searches for physics beyond the Standard Model using QCD-multijet events, e. g. [3].

In the here presented analysis, the first measurement of the data-to-simulation resolution ratio  $\sigma_{\text{JER}}^{\text{data}}/\sigma_{\text{JER}}^{\text{MC}}$  using  $\gamma + \text{jet}$  events with  $19.7 \text{ fb}^{-1}$   $pp$ -collision data at  $\sqrt{s} = 8 \text{ TeV}$  collected in 2012 at the CMS detector was carried out. For this purpose, the methodology introduced in [6, 7] was further developed. To take account of the double peak structure when applying an exclusive binning in the variable  $\alpha$  which measures the additional jet activity in the event, the event selection explicitly distinguishes the case of parton radiation in the leading jet/photon hemispheres. This change in methodology is introduced for the first time by this measurement.

The resolution in data is found to be systematically larger than in simulation throughout



the investigated  $\eta^{\text{jet}}$  plane. A possible  $p_{\text{T}}^{\gamma}$  dependence of the resolution scale factors  $\rho_{\text{res}}$  is not visible. Thus, the ratio is parametrised with a constant per  $\eta^{\text{jet}}$ -bin.

The relative difference of the data resolution ranges from  $\sim 7\%$  to  $\sim 20\%$  for  $|\eta^{\text{jet}}|$  between  $0.0 - 0.5$  and between  $1.7 - 2.3$ , respectively, with total statistical and systematic uncertainties between  $3\%$  and  $8\%$ .

The here presented measurement serves as a cross-check measurement to the jet- $p_{\text{T}}$  resolution ratio result using dijet events [8, 16]. Both measurements are compatible within their statistical and systematic uncertainties.

For a future measurement, a reduction of the uncertainties is desirable. Since the systematic uncertainty is still dominating, most notably the uncertainty on the simulation of out-of-cone showering, an improved evaluation of the out-of-cone showering uncertainty could significantly improve the precision of the data-to-simulation ratio  $\sigma_{\text{JER}}^{\text{data}}/\sigma_{\text{JER}}^{\text{MC}}$ . A better evaluation can be possibly achieved by a better understanding, whether the difference of  $\rho_{\text{res}}$  using clustered jets within a radius of  $0.7$  and  $0.5$  is only originating from out-of-cone showering effects. Since the simulation of out-of-cone showering should in principal only enter the result by the residual imbalance  $q$ , an overestimation by the here presented method might be possible.

Furthermore, an increase in the statistical precision is desirable to allow for the coverage of the measurement of the resolution scale factors in the high pseudorapidity regions which has not been possible so far.



## A Measurement of the jet transverse-momentum resolution

### A.1 Pileup reweighting

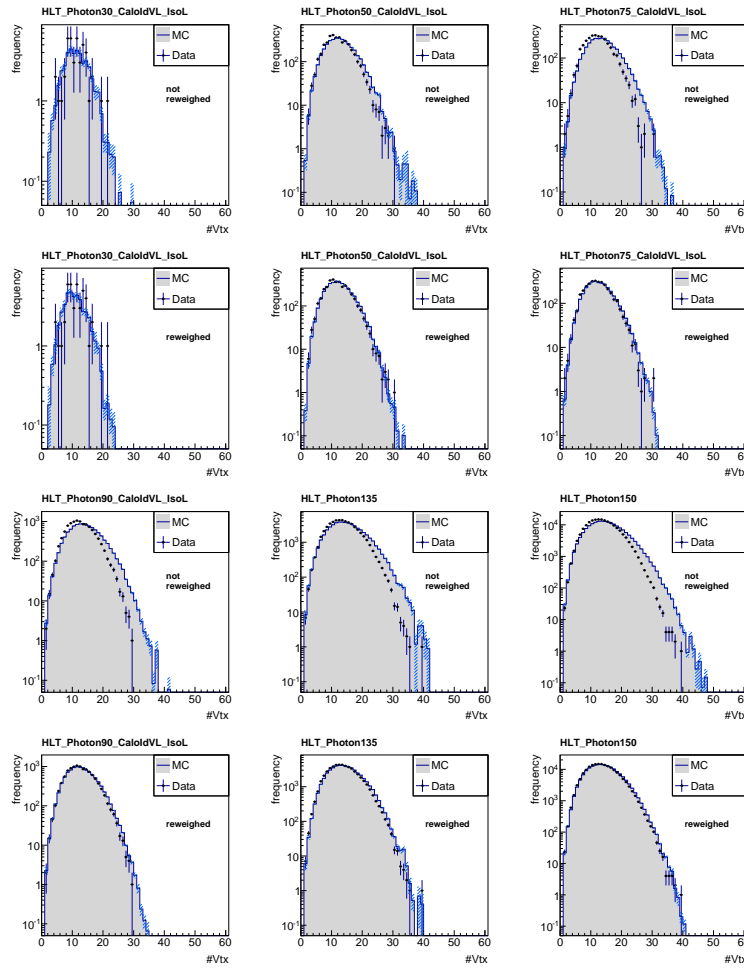


Figure A.1: The number of primary vertices in data and simulation before (1st row) and after (2nd row) pileup reweighting for  $36 \text{ GeV} < p_T^\gamma < 60 \text{ GeV}$  (left),  $60 \text{ GeV} < p_T^\gamma < 88 \text{ GeV}$  (middle), and  $88 \text{ GeV} < p_T^\gamma < 105 \text{ GeV}$  (right) and the number of primary vertices in data and simulation before (3rd row) and after (4th row) pileup reweighting for  $105 \text{ GeV} < p_T^\gamma < 149 \text{ GeV}$  (left),  $149 \text{ GeV} < p_T^\gamma < 165 \text{ GeV}$  (middle), and  $165 \text{ GeV} < p_T^\gamma$  (right).

558

## A.2 Summary of all selection requirements

Table A.1: Summary of all selection criteria for the measurements of the jet transverse-momentum resolution with  $\gamma + \text{jet}$  events.

|                       |   |
|-----------------------|---|
| One jet with          | $p_T > 10 \text{ GeV}$<br>Neutral hadron fraction $< 0.90$<br>Neutral electromagnetic fraction $< 0.90$<br>Number of constituents $> 1$<br>Charged hadron fraction $> 0$<br>Charged hadron multiplicity $> 0$   |
| One photon with       | $p_T > 22 \text{ GeV}$<br>$ \eta  < 1.3$<br>$\frac{H}{E} < 0.05$<br>$\sigma_{in\eta} < 0.013$<br>ECAL isolation $< 4.2 \text{ GeV} + 0.0060 \cdot p_T^\gamma$<br>HCAL isolation $< 2.2 \text{ GeV} + 0.0025 \cdot p_T^\gamma$<br>Track Isolation $< 2.0 \text{ GeV} + 0.0010 \cdot p_T^\gamma$<br>Pixel seed veto |
| Event-based selection | $p_T^{2^{\text{nd}} \text{ jet}} > 10 \text{ GeV}$<br>$\frac{p_T^{2^{\text{nd}} \text{ jet}}}{p_T^\gamma} < 0.20$<br>$\Delta\Phi(1^{\text{st}} \text{ jet}, \gamma) > 2.95$   |

559

## A.3 Generator-level jet flavor definition

560

The algorithmic flavor definition uses the following discrimination:

561

- Try to find the parton that most likely determines the properties of the jet and assign that flavor as true flavor

562

- Here, the “final state” partons (after showering, radiation) are analyzed (also within  $\Delta R < 0.3$  of reconstructed jet cone)
- Jets from radiation are matched with full efficiency
- If there is a b/c within the jet cone: label as b/c
- Otherwise: assign flavor of the hardest parton

## A.4 Extrapolation plots

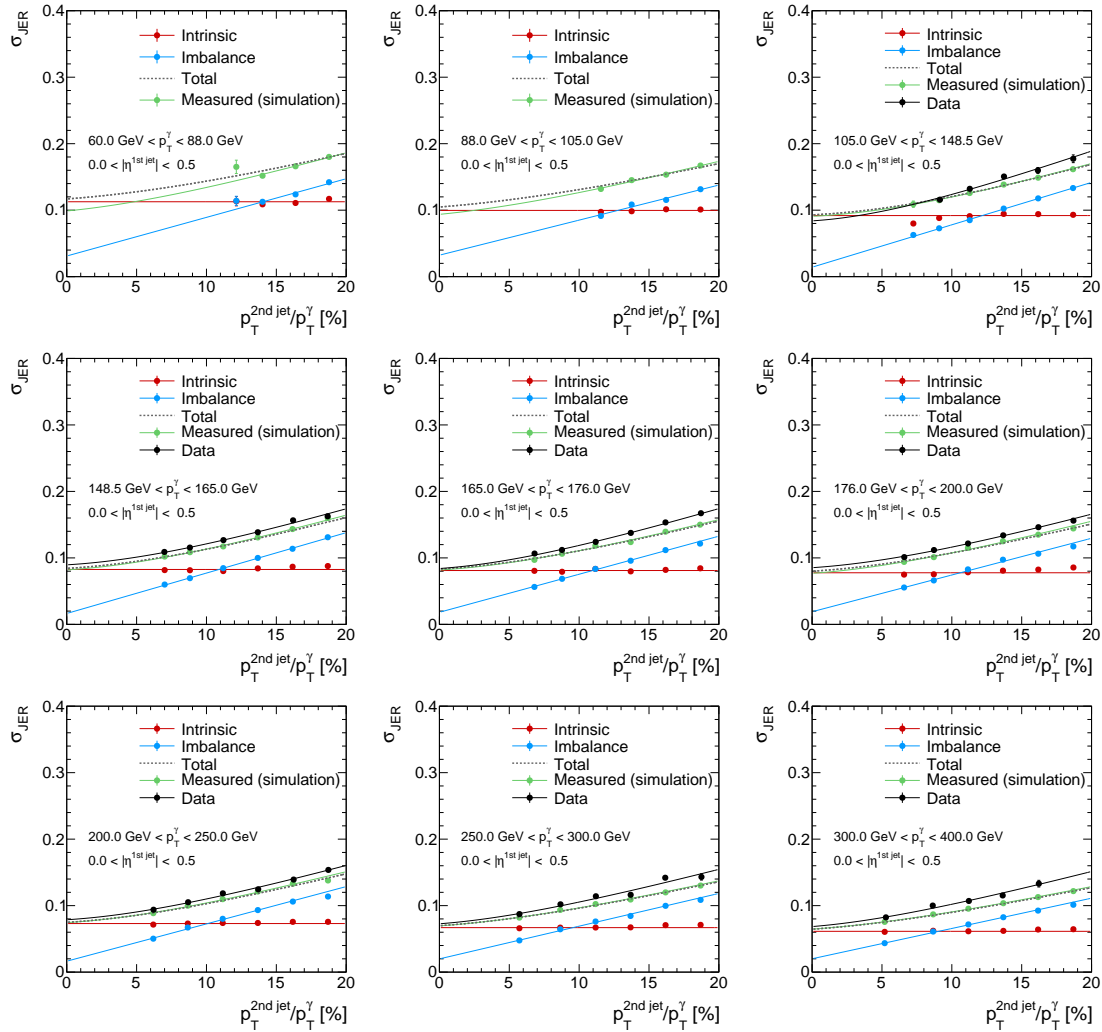


Figure A.2:  $\sigma_{\text{JER}}$  ( $\alpha$ ) of the intrinsic, imbalance and measured resolution in simulation and the resolution measured in data for all  $|\eta^{1\text{st jet}}|$  and  $p_T^\gamma$  bins.

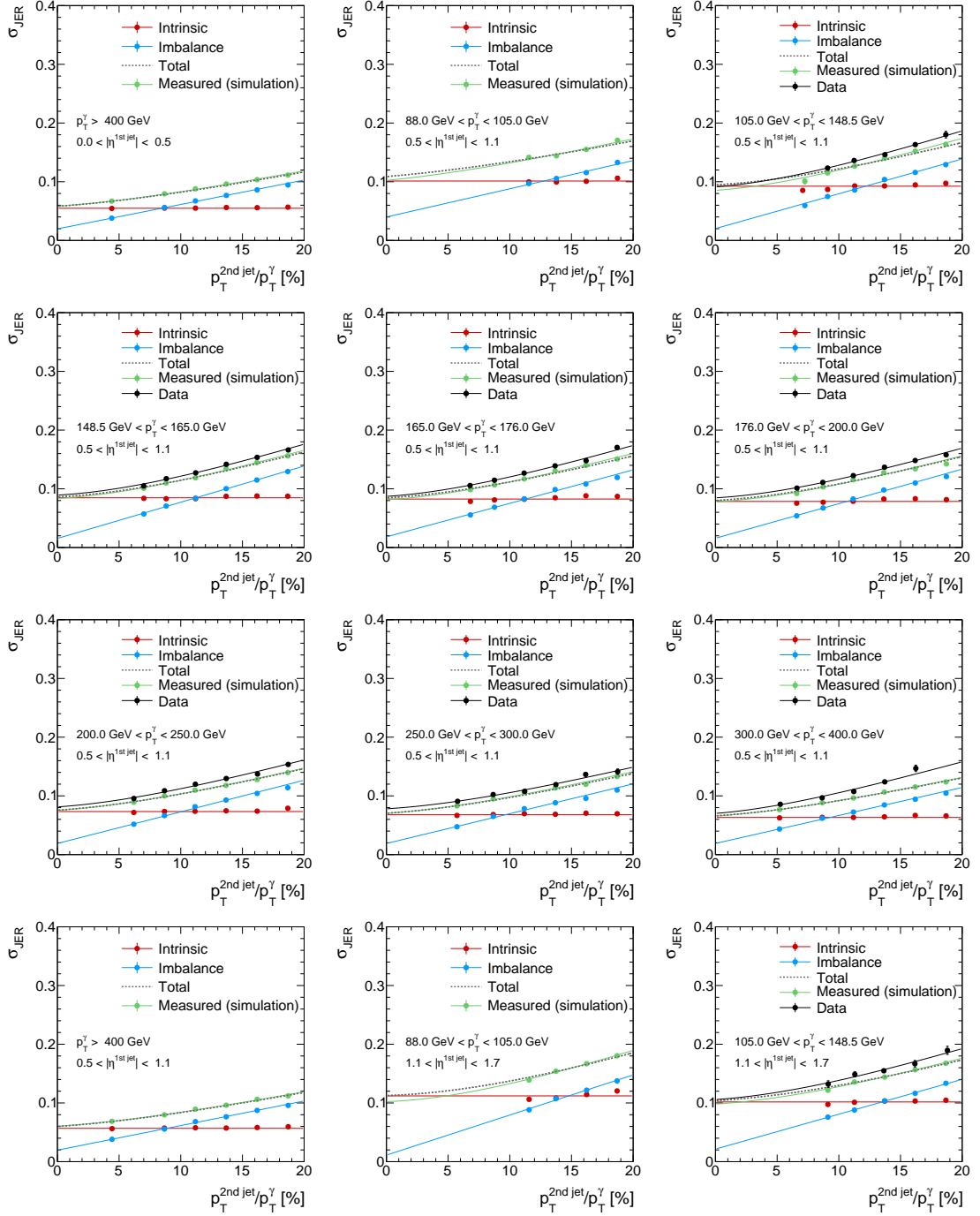


Figure A.3: Continued from Fig. A.2:  $\sigma_{JER}$  ( $\alpha$ ) of the intrinsic, imbalance and measured resolution in simulation and the resolution measured in data for all  $|\eta^{1st\ jet}|$  and  $p_T^\gamma$  bins.

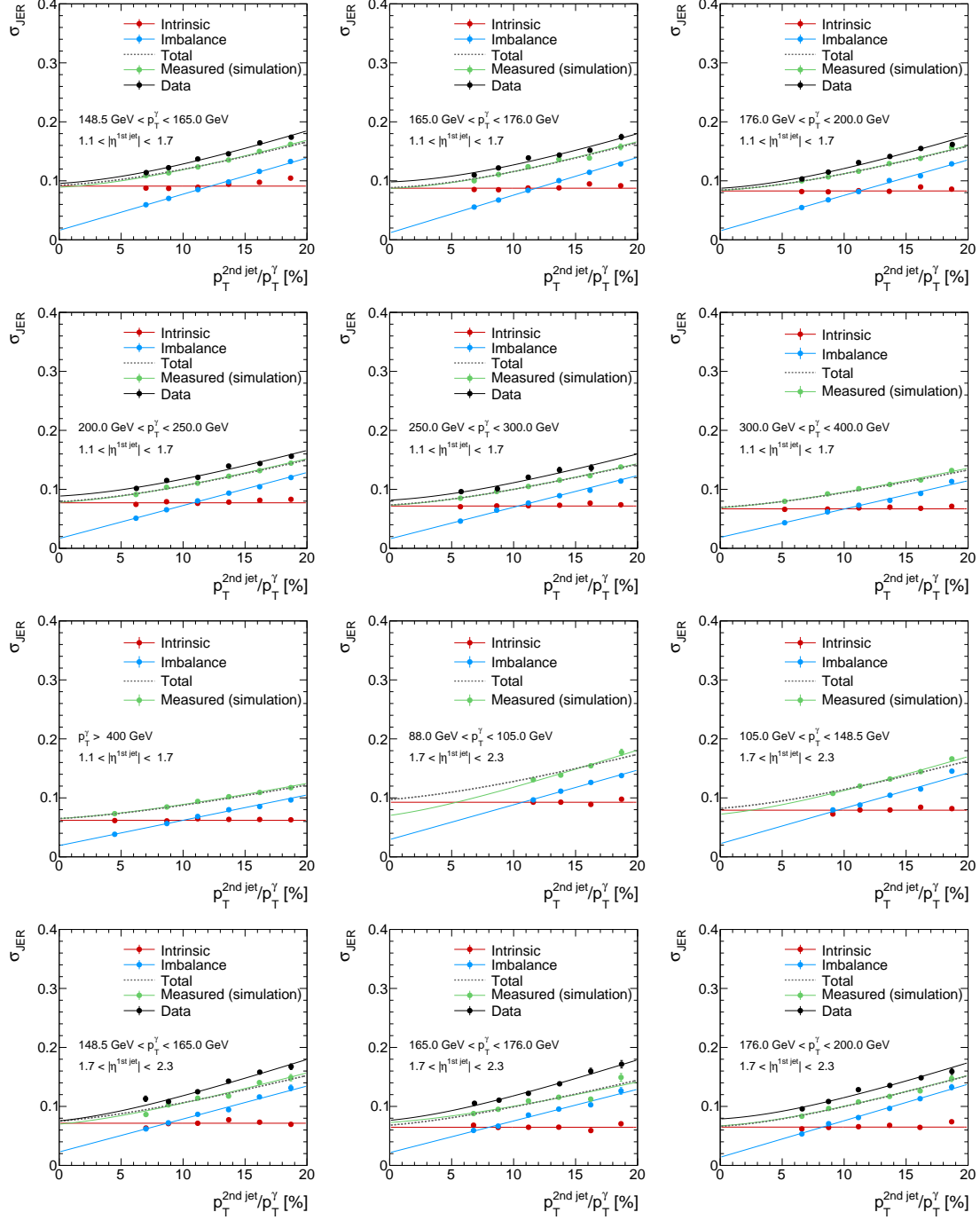


Figure A.4: Continued from Fig. A.3:  $\sigma_{\text{JER}}(\alpha)$  of the intrinsic, imbalance and measured resolution in simulation and the resolution measured in data for all  $|\eta^{1\text{st jet}}|$  and  $p_T^\gamma$  bins.

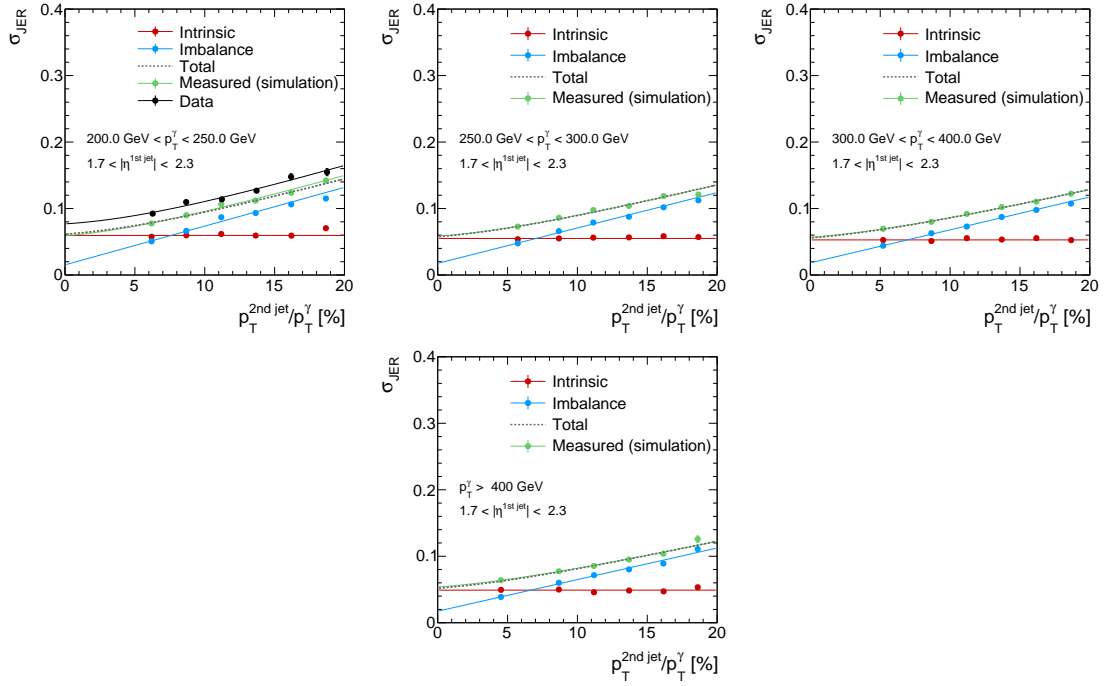


Figure A.5: Continued from Fig. A.4:  $\sigma_{\text{JER}}(\alpha)$  of the intrinsic, imbalance and measured resolution in simulation and the resolution measured in data for all  $|\eta^{1\text{st jet}}|$  and  $p_T^\gamma$  bins.



## Bibliography

- [1] CMS Collaboration, “Measurements of differential dijet cross section in proton-proton collisions at  $\sqrt{s} = 8$  TeV with the CMS detector”, *CMS Physics Analysis Summary CMS-PAS-SMP-14-002* (2014).
- [2] CMS Collaboration, “Measurement of the differential cross section for top quark pair production in pp collisions at  $\sqrt{s} = 8$  TeV”, *Eur. Phys. J. C* **75** (2015), no. 11, 542, [arXiv:1505.04480](#). doi:10.1140/epjc/s10052-015-3709-x.
- [3] CMS Collaboration, “Search for new physics in the multijet and missing transverse momentum final state in proton-proton collisions at  $\sqrt{s} = 8$  TeV”, *JHEP* **06** (2014) 055, [arXiv:1402.4770](#). doi:10.1007/JHEP06(2014)055.
- [4] CMS Collaboration, “Searches for Supersymmetry using the  $M_{T2}$  Variable in Hadronic Events Produced in pp Collisions at 8 TeV”, *JHEP* **05** (2015) 078, [arXiv:1502.04358](#). doi:10.1007/JHEP05(2015)078.
- [5] CMS Collaboration, “Search for supersymmetry in hadronic final states with missing transverse energy using the variables  $\alpha_T$  and b-quark multiplicity in pp collisions at  $\sqrt{s} = 8$  TeV”, *Eur. Phys. J. C* **73** (2013), no. 9, 2568, [arXiv:1303.2985](#). doi:10.1140/epjc/s10052-013-2568-6.
- [6] CMS Collaboration, “Determination of Jet Energy Calibration and Transverse Momentum Resolution in CMS”, *JINST* **6** (2011) P11002, [arXiv:1107.4277](#). doi:10.1088/1748-0221/6/11/P11002.
- [7] CMS Collaboration, “Jet Energy Resolution in CMS at  $\sqrt{s} = 7$  TeV”, *CMS Physics Analysis Summary CMS-PAS-JME-10-014* (2011).
- [8] CMS Collaboration, “Jet Energy Scale and Resolution in the CMS Experiment”, *CMS Physics Analysis Summary CMS-PAS-JME-13-004* (2015).
- [9] M. Schröder, “Quality of jet measurements and impact on a search for new physics at CMS”. PhD thesis, Hamburg U., 2012.  
<http://www-library.desy.de/cgi-bin/showprep.pl?thesis12-042>.
- [10] CMS Collaboration, “Performance of Photon Reconstruction and Identification with the CMS Detector in Proton-Proton Collisions at  $\sqrt{s} = 8$  TeV”, *JINST* **10** (2015), no. 08, P08010, [arXiv:1502.02702](#). doi:10.1088/1748-0221/10/08/P08010.

- [11] CMS Collaboration, “Particle-Flow Event Reconstruction in CMS and Performance for Jets, Taus, and MET”, *CMS Physics Analysis Summary* **CMS-PAS-PFT-09-001** (2009).
- [12] M. Cacciari, G. P. Salam, and G. Soyez, “The anti- $k_t$  jet clustering algorithm”, *JHEP* **04** (2008) 063, [arXiv:0802.1189](#). doi:10.1088/1126-6708/2008/04/063.
- [13] N. Odell, “PF Jet ID Recommendation”.  
[https://indico.cern.ch/event/89919/contribution/0/attachments/1091238/1556772/PF\\_JET\\_ID\\_Reccomendation.pdf](https://indico.cern.ch/event/89919/contribution/0/attachments/1091238/1556772/PF_JET_ID_Reccomendation.pdf), April, 2010.
- [14] N. Saoulidou and E. Tziaferi, “Performance of the Particle-Flow jet identification criteria using proton-proton collisions at  $\sqrt{s} = 8\text{ TeV}$ ”, *CMS Analysis Note* **CMS-AN-14-227** (2014). Internal documentation.
- [15] CMS Collaboration, “Isolated Photon Reconstruction and Identification at  $\sqrt{s} = 7\text{ TeV}$ ”, *CMS Physics Analysis Summary* **CMS-PAS-EGM-10-006** (2011).
- [16] K. Goebel, “Probing supersymmetry based on precise jet measurements at the CMS experiment”. PhD thesis, U. Hamburg, Dept. Phys., 2015.  
<http://www-library.desy.de/cgi-bin/showprep.pl?thesis15-003>.

